Results in Chemistry 18 (2025) 102706

Contents lists available at ScienceDirect

Results in Chemistry

journal homepage: www.sciencedirect.com/journal/results-in-chemistry

Understanding of the optical/photocatalytic properties of bismuth oxyiodide with reduced graphene oxide

Lisdelys González-Rodríguez [a,b,*], Osvaldo Yañez [a], David Contreras [c], Yoan Hidalgo-Rosa [d,e], Ximena Zarate [f], Mario Saavedra-Torres [f], Eduardo Schott [g], Carolina Baeza [h], Udayabhaskar Rednam [i], R.V. Mangalaraja [j], Daniel Mondaca [k]

[a] Centro de Modelación Ambiental y Dinámica de Sistemas (CEMADIS), Facultad de Ingeniería y Negocios, Universidad de Las Américas, Santiago 7500975, Chile
[b] Facultad de Ingeniería y Negocios, Universidad de las Américas, Sede Concepción, Concepción, Chile
[c] Departamento de Química Analítica e Inorgánica, Facultad de Ciencias Químicas, Universidad de Concepción, Chile
[d] Centro de Nanotecnología Aplicada, Facultad de Ciencias, Ingeniería y Tecnología, Universidad Mayor, Camino La Pirámide 5750, Huechuraba, Santiago 8580745, Chile
[e] Escuela de Ingeniería del Medio Ambiente y Sustentabilidad, Facultad de Ciencias, Ingeniería y Tecnología, Universidad Mayor, Camino La Pirámide 5750, Huechuraba, 8580745 Santiago, Chile
[f] Instituto de Ciencias Aplicadas, Facultad de Ingeniería, Universidad Autónoma de Chile, Av. Pedro de Valdivia 425, Santiago, Chile
[g] Departamento de Química Inorgánica, Facultad de Química Y de Farmacia, Centro de Energía UC, Centro de Investigación en Nanotecnología y Materiales Avanzados CIEN-UC, Pontificia Universidad Católica de Chile, Avenida Vicuña Mackenna, 4860 Santiago, Chile
[h] Facultad de Ciencias Ambientales, Universidad de Concepción, Concepción, Chile
[i] Departamento de Mecánica, Facultad de Ingeniería, Universidad Tecnológica Metropolitana, Santiago, Chile
[j] Vicerrectoría de Investigación e Innovación, Universidad Arturo Prat, Avenida Arturo Prat 2120, Iquique 1110939, Chile
[k] Departamento de Geología, Facultad de Ciencias Físicas y Matemáticas, Universidad de Chile, Santiago de Chile, Chile

ARTICLE INFO

Keywords:
BiOI-based materials
Reduced graphene oxide
Heterogeneous photocatalysis
DFT studies

ABSTRACT

Semiconductor photocatalysis has attracted great interest because it offers a promising approach to solving environmental aquatic pollution. This study comprehends a synthesis via the reflux method for obtaining Bismuth Oxyiodide (BiOI) and BiOI joined at reduced graphene oxide (BiOI/rGO). The materials were studied using different experimental and theoretical techniques including X-ray diffraction, N_2 adsorption-desorption isotherms, SEM, TEM, Raman, DRS, and density functional theory calculations (DFT). The results indicated that BiOI/rGO has a crystal structure considerably stable, where interplanar spacing and the lattice parameters experienced only slight changes. Experimental and theoretical results show that electronic interaction between rGO sheet and BiOI reduced the band-gap, but in the case of DFT underestimation of band-gap values. DFT analysis showed the role of the hydroxyl group and epoxy groups in the charge transfer along the interfacial direction of heterostructure BiOI/rGO. The adsorption-photocatalytic ability of BiOI/rGO was 2.5 times higher than the pristine BiOI. This study underscores the importance of material design in enhancing photocatalytic applications, paving the way for further research into similar composites for environmental remediation. The developed material will provide a novel strategy to facilitate the treatment of polluted waters in modern environmental engineering.

1. Introduction

Semiconductor photocatalysis has attracted great interest because it offers a promising approach to solving energy supply and environmental aquatic pollution [1]. Among them, the great family of Bismuth Oxyhalides (BiOX, X: Cl, Br, I) attracts wide attention for their unique layered structure [1–3]. Particularly the bismuth oxyiodide (BiOI) distinguish due to the smallest band-gap which allows strong absorption in the visible-light region [4]. By selecting appropriate fabrication strategies (e.g., chemical oxidative polymerization, thermal reduction,

* Corresponding author at: Centro de Modelación Ambiental y Dinámica de Sistemas (CEMADIS), Facultad de Ingeniería y Negocios, Universidad de Las Américas, Santiago 7500975, Chile.
E-mail address: lgonzalezr@udla.cl (L. González-Rodríguez).

https://doi.org/10.1016/j.rechem.2025.102706
Received 15 July 2025; Accepted 12 September 2025
Available online 18 September 2025

reflux, hydrothermal or solvothermal methods), researchers can independently control material morphology and properties, resulting in materials designed for targeted applications like environmental sensing, energy harvesting, or pollution remediation [5–11]. For example, balancing the BiOI content and precisely controlling the fabrication conditions are fundamental for maximizing the desired nanocomposite properties and efficiency across electrical, optical, and piezoelectric domains [5]. Other researchers [12] showed that the ability of BiOI nanoflakes synthetized via chemical method is a promising candidate for degrading Methyl Blue under ultraviolet light. The smaller band gap of BiOI enables it to absorb a wider range of light, including visible light, which is crucial for many photocatalytic applications. Besides, BiOI nanoflakes, being two-dimensional nanomaterials, naturally possess a high surface area to volume ratio. This provides more sites for pollutants to attach and be adsorbed, promoting their degradation.

Moreover, the crystallite structure has a significant role, different exposed facets are highly oriented in the (001) or (110) facets and 3D microspheres often exhibit enhancement photocatalytic properties [6,13–16]. Recently, many researchers have focused on the synthesis of different facets in some BiOX [17] [18]. For example, Jiang et al. [19] and Li et al. [20] reported that the BiOCl nanosheets with exposed (010) facets had better photocatalytic activity than (001) facets under visible light. The BiOBr nanosheets reported by [17] with dominantly exposed (102) and (001) facets have more efficient electron injection, the higher redox potential of the photoinduced hole, and a smaller band-gap. Two studies by [21,22] illustrate the use of crystal facet engineering to promote photocatalytic performance. Therefore, facet engineering of BiOI with the exposed proportion of (001), (110), and (102) facets can facilitate effective separation of the photo generated. Thus, a lower recombination rate increases photocatalytic reactions. However, in some studies the BiOI system has been recognized by the rapid recombination of electron-hole pairs, thus greatly reducing their photochemical performance [23,24]. To overcome this limitation, the BiOI has been modified with inorganic materials, including reduced graphene oxide (rGO) [7,25–27]. BiOI combined with rGO has garnered attention for its enhanced optical and photocatalytic properties [7]. This combination is promising for applications in environmental remediation and energy conversion. rGO is a low-cost material that has an adequate band separation, appropriate band gap, high mobility of the carrier, and chemical stability [28,29]. In this sense, the hybridization between BiOI/rGO can facilitate the migration of interfacial charge carriers, suppresses the charge recombination [30], and suitable band-gap [7,27], improving the separation of photogenerated electron-hole pairs in BiOI, thus enhancing photocatalytic efficiency. The composite shows increased reactivity under visible light, making it effective for degrading organic pollutants. The incorporation of rGO can enhance the structural stability of BiOI under operational conditions, reducing degradation during photocatalytic reactions.

Density Functional Theory (DFT) is a powerful computational tool used to investigate the electronic properties and stability of materials [31–33]. Proper assessment of the band-gap is one of the major challenges of the DFT methods due to the great size of these materials, which implies high computing times and computational resources according to the theoretical level used. However, several studies based on DFT calculations have been reported, providing a more detailed description, for instance, the band offsets and electronic behavior in the interface of the heterostructures [30,34,35]. To calculate the band structure and density of states (DOS) of BiOI/rGO composites, researchers employ various computational methods rooted in DFT and, in some cases, other advanced quantum-chemical techniques. The Quantum Theory of Atoms in Molecules (QTAIM) analysis provides a detailed understanding of the interactions between BiOI and rGO, revealing the nature and strength of bonding interactions [36]. This research [36], discusses a novel methodology for analyzing noncovalent interactions in complex biological systems, allows us to investigate the electronic structure and bonding characteristics at a molecular level. Recently in [37,38] simulations were used to visualize the adsorption process and assess the stability of the metal-silicate complexes. By integrating these models, researchers can improve the accuracy of computational predictions regarding stability and binding affinities in different complexes. In addition, estimating several topological properties at Bond Critical Points (BCPs), we can better understand the stability and reactivity of the BiOI/rGO interface, which is crucial for optimizing several chemical processes such as adsorption and solar photocatalysis. Understanding these interactions is crucial for predicting the material's properties and potential applications in these fields.

For this reason, there were investigated the important properties, such as structural, electronic, and photocatalytic properties of BiOI/rGO using experimental studies along with theoretical tools.

Hence, this work was performed to develop a facile and eco-friendly reflux method to produce BiOI and BiOI/rGO materials. To understand the structural, optical changes, and photocatalytic properties of graphene loading different experimental and theoretical techniques including X-ray diffraction, N_2 adsorption-desorption isotherms, SEM, TEM, Raman, DRS, and DFT were used. Finally, the materials were tested to evaluate photocatalytic properties. The results show that the proposed new modified material enhancement of photocatalytic degradation provides better degradation to facilitate the treatment of pollutant waters in environmental engineering.

2. Materials and method

2.1. Computational details

BiOI cell parameters were optimized according to the simple tetragonal shape P4/nmm, resulting in a, b = 3.93 Å and c = 8.15 Å, $\alpha = \beta = \gamma = 90^{\circ}$ which are in good agreement and on a range of experimental data [39,40]. Bulk for BiOI (001) was optimized with 5x5x5 k-points mesh for Brillouin sampling. BiOI slab cell models were constructed using 2 layers. rGO was modeled through a graphene structure, which was built considering the graphite hexagonal crystal, being optimized with a = 2.465, showing good parameters with experimental data (a = 2.461) [41]. A cage c3x2 of graphite (001) was used to attach oxygen and hydrogen atoms, according to the proportion of elements given here (see the experimental data). Periodic cell dimensions were adjusted to get the BiOI and rGO interacting system. The rGO was placed facing the BiOI at an initial distance of 3 Å and to avoid the interaction of adsorbate between replicas, a vacuum of 10 Å in the *Z*-axis direction was included.

All calculations were modeled using Perdew-Burke-Ernzerhof (PBE) functional, [42] with GBRV 1.5 pseudopotentials [43] and considering an energy-cutoff of 45 Ryd. A 5x5x1 k-points mesh was used for all optimizations. Electronic calculations as Density of states (DOS) were performed with a 10x10x1 k-point mesh. Dipole corrections [44] were applied to compensate for artificial electric fields caused by periodic boundary conditions, and Grimme-D3 modified dispersion with Becke-Johnson damping correction (D3M-BJ) [45] was also included in all calculations. All computations were performed using the Quantum Espresso 6.5 package [46,47]. Figures have been represented through VESTA software [48].

We performed the electron density difference ($\Delta\rho$) analysis [49] on the complex (BiOI/rGO). The $\Delta\rho$ is defined according to eq. 1. In the equation, $\Delta\rho$(BiOI+rGO) represents the density difference of the complex, while ρ(BiOI) and ρ(rGO) represent the atomic density of BiOI and rGO, respectively.

$$\Delta\rho(\mathrm{BiOI/rGO}) = \rho(\mathrm{BiOI + rGO}) - \rho(\mathrm{BiOI}) - \rho(\mathrm{rGO}) \quad (1)$$

To get an idea of the 350 cm^{-1} Raman intensity unknown, we performed a frequencies analysis of the resultant complexes, applying discrete molecular techniques through PBE functional [50] in combination with def-SVPP [51] all-electron basis set for light elements (C, O, H) and LANL2DZ pseudopotential for Bi and I elements, [52] using Gaussian09 software package [50–52].

The discrete molecular modeling of BiOI began by adapting the BiOCl structure from The Materials Project (ID: mp-22,939), substituting chlorine with iodine. The rGO surface was constructed using ChemAxon's MarvinSketch module (https://chemaxon.com/marvinsketch_js). Both structures underwent optimization using the GFN2-xTB Hamiltonian semi-empirical tight-binding method [53] implemented in the xTB software [54], confirming stability through the absence of imaginary frequencies. The BiOI was then positioned on the rGO surface using (Visual Molecular Dynamics) VMD software [55]. Van der Waals radii guided the optimal distance between structures, and the resulting BiOI/rGO complex underwent further geometry optimization with the GFN2-xTB Hamiltonian. Following optimization, a molden file containing wavefunction information was generated to perform HOMO-LUMO orbital calculations, Independent Gradient Model based on Hirshfeld partition (IGMH) [36,56,57], and Quantum Theory of Atoms in Molecules (QTAIM) [58,59]. We developed an IGMH to analyze intramolecular and intermolecular interactions. IGMH enhances the existing Independent Gradient Model by incorporating Hirshfeld partitioning of molecular density instead of free-state atomic densities, providing a more rigorous physical foundation. To comprehensively understand BiOI/rGO interactions, we conducted a QTAIM analysis, developed by Bader [60]. This approach examines molecular structure and bonds based on total electron density, enabling estimation of key topological properties at Bond Critical Points (BCPs), including electron density (ρ), potential energy density V(r), total energy density H(r), laplacian of electron density ($\nabla^2\rho$), lagrangian kinetic energy G(r), sign(λ_2)ρ, and the δg function defined in IGMH partition. These properties provide valuable insights into the nature of interactions. Both IGMH and QTAIM analyses were performed at the GFN2-xTB Hamiltonian level using Multiwfn software [61], with molecular visualization conducted using VMD.

Additionally, molecular dynamics simulations were performed employing the GFN2-xTB Hamiltonian to assess kinetic stability and explore conformational space. The simulations ran for 30 ps, aiming to reach equilibrium., within a constant number of atoms, volume, and temperature (NVT) ensemble, equations of motion were integrated using a 1.0 femtosecond time step at 300 K. Temperature was maintained using a Berendsen thermostat [62,63], while the SHAKE algorithm ensured hydrogen atom stability. Data collect occurred every 1 fs throughout the simulation, enabling thorough exploration of the system's conformational space and allowing molecules to achieve stable equilibrium states.

2.2. Experimental details

2.2.1. Chemicals

The chemical reagents employed were: $KMnO_4$, H_2SO_4, H_2O_2, potassium iodide KI 99 %; TiO_2 Degussa P-25®, NaOH; HNO_3 65 %; Methanol grade HPLC and bismuth nitrate pentahydrate $Bi(NO_3)_3$*$5H_2O$ 98 %; NaH_2PO_4 monobasic 98 %; H_3PO_4, Ethanol. All reagents were obtained from brands Sigma-Aldrich and Merck. Nanopure water is used throughout the experiments (Nanopure System, Models D4752 Barnstead).

2.2.2. Synthesis method

Reduced Graphene Oxide (rGO) was set from prepared GO powders reported elsewhere [64]. Expanded graphite was used as a precursor in the synthesis of rGO. Expanded graphite (1 g) was mixed with 3 g of $KMnO_4$, then, 20 mL of H_2SO_4 was added and stirred for 15 min. It went on to be treated at 35 °C, stirring for 30 min which resulted in the formation of a thick paste. 100 mL of ultrapure water was added under rapid stirring. The mixture kept constantly stirring at 85 °C for 1 h and, 10 mL of H_2O_2 was added. The final mixture was passed through a testing sieve (Advantech Manufacturing, USA, U.S. Standard Testing Sieve, 300 mm pore size) and the solid precipitate was washed and dried. The properties of rGO are better than those of GO because of the diminished number of oxygenated groups and defects [65]. To prepare BiOI/rGO material whit a percent difference of rGO the process for the first trial was as follows, take 50 ml of ethanol as solvent, to this add 0.3 g of $Bi(NO_3)_3$*$5H_2O$ 98 %, stir vigorously for ~30 min at room temperature. Wang et al. [66] reported that using ethanol solvent changes the surface reaction sites and improves the photocatalytic properties of BiOI. For better dispersion, use the bath sonicated. Add 10 % rGO and mass of KI, under continuous stirring till brown precipitate forms. The mixture for 8 h under reflux conditions at 60 °C. The solution obtained was filtered and the precipitate was washed thoroughly with distilled water and absolute ethanol several times and then dried at 60 °C overnight. To compare, pure BiOI was synthesized. The BiOI was prepared without the addition of rGO via the same reflux method.

2.2.3. Instruments and calculations

The XRD patterns were recorded using an Advance diffractometer Bruker D4 with CuKα radiation (λ = 0.154 nm). The range of 2θ was scanned between 5° and 80° at a speed of 0.02°/s. The identification of the phases was achieved by the "Crystallography Open Database" (COD, http://www.crystallography.net/cod/), [67,68]. To compare the influence of the rGO on the structural properties of BiOI, XRD patterns were analyzed to obtain interplanar spacing, crystallite size, and other lattice parameters. The interplanar spacing of the tetragonal lattice and average crystal size for this plane using the Debye Scherrer were obtained using the eqs. (2–3) [69].

$$\frac{1}{d_{hkl}^2} = \frac{(h^2 + k^2)}{a^2} + \frac{l^2}{c^2} \tag{2}$$

$$D = \frac{K\lambda}{\beta \cos\theta} \tag{3}$$

where h, k, and l, are the Miller indexes and a and c are the lattice parameters of the tetragonal lattice. The interlayer distance (d) was found using the Bragg eq. K is the shape factor with a value of 0.94, β is the full width at half maximum (FWHM value in radian) of the diffraction major line, and θ is the Bragg angle. The XRD data of the samples were fitted with a Gaussian profile to get the exact peak positions and FWHM from OriginPro 2021 9.8.0.200 software.

The surface area of the samples was determined using a BELSORP-mini II surface area and pore size. The Barrett-Joyner-Halenda (BJH) method was employed to calculate the pore size. For investigating morphology, scanning electron microscopy (SEM and EDS) was used through a VEGA3 EASYPROBE SBU (TESCAN). TEM micrographs were obtained using a JEM 1200EX 11, JEOL transmission electron microscopy (Germany) with an F82 camera (Gatan, USA). The Raman was carried out using a LabRAM HR Evolution coupled with laser HeNe 633 nm/17 mW y DuoScan-HR, while the UV–Visible diffuse reflectance spectra (DRS) were obtained from an Evolution 260 Bio UV–vis spectrophotometer (Thermo Fisher Scientific Inc.) equipped with an integrating sphere in the range of 290–1100 nm, with a spectral resolution of 1 nm. The band-gap energy (E_g) is determined by Tauc relation, which is given by: $h\nu\alpha^{\frac{1}{n}} = A(h\nu - E_g)$, where h is Planck's constant, ν is the light frequency, α is the absorption coefficient, and A is a proportional constant. The value of n denotes the nature of the simple transition. For an indirect allowed transition, $n = 2$. The α in the Tauc equation is substituted with the Kubelka–Munk function, F(R∞) [70]. The estimation of energy of the valence band (E_{vb}) was obtained following the empirical eq. 4 [71,72] where χ is the semiconductor electronegativity, which is defined as the geometric mean of the electronegativity of the constituent atoms (5.94 eV for BiOI) and (5.81 eV TiO_2) [73], E_e is the energy of free electrons on the hydrogen scale (~4.5 eV), and E_g is the band-gap energy of the semiconductor. The energy of conduction band E_{cb} was obtained considering eq. 5.

$$E_{vb} = \chi - E_e + 0.5\, E_g \tag{4}$$

$$E_{cb} = E_{vb} - E_g \quad (5)$$

2.2.4. Photocatalytic tests

To evaluate the photocatalytic performance of the materials was selected methyl orange (MO). This pollutant is very stable to light and difficult to be decomposed [74]. Photocatalytic and photolysis experiments were conducted in a batch small-scale photoreactor. For the photocatalytic measurement, the as-synthetized samples (30 mg) were dispersed in 100 mL MO aqueous solutions with a concentration of 13 mg/L (41.9 umol/L), (pH 5.7–6.0) at this pH range the anionic form is predominant. Before irradiation, the suspension was stirred in the dark to establish an adsorption/desorption equilibrium. Then the suspension was exposed to visible light irradiation generated by a 400 W metal halide lamp (Osram Powerstar HQI–E400 W/D Pro Daylight). The wavelength distribution and light intensity are shown in **(Figure SI1 of the Supporting Information).** The emission spectrum of the lamp was recorded with a fluorescence spectrometer (LS–45, PerkinElmer) in luminescence mode. The radiant flux of the lamp was 2559 ± 44 μEinstein m^{-2} s^{-1}; this flux was recorded for 3 h using a QSPL-2100 radiometer (Biospherical Instruments Inc) with a quantum response from 400 to 700 nm. The temperatures inside the photocatalytic reactor reached 37 ± 2 °C. 1 ml suspension was sampled at given time intervals and then separated by filtering to remove the solid particles and analyzed by measuring the absorption intensity at a maximum absorbance wavelength of λ = 464 nm using UV–vis spectrophotometry (Agilent 8453 diode array spectrophotometer) with a 1 cm path length spectrometric quartz cell. Photocatalytic efficiency (PE, %) was determined by eq. 6. C_f is the remaining MO concentration and C_0 is the initial MO concentration after adsorption-desorption equilibrium in the dark. Error bars represent the standard deviation (SD) calculated from replicating three experiments. All experiments were carried out using TiO_2 Degussa P25 and rGO like positive and negative control test respectively.

$$PE\ (\%) = \frac{C_o - C_f}{C_0} x\ 100 \quad (6)$$

3. Results and discussion

3.1. Computational results

Based on the results, we proceeded to analyze the charge transfer and interface interaction of heterostructure BiOI/rGO through DFT methods. In this sense, the analysis of the density of states (DOS) was used to further insight into the change of the position of E_{vb} and E_{cb} of BiOI and rGO after contact and the projected density of state (PDOS) was obtained to analyze the composition of the bands. On the other hand, interfacial charge transfer is known to play an important role in photocatalytic activity as the systems may decrease the energy gap and take better advantage of visible light [30,75]. From this perspective, the electron density difference analysis was carried out in the framework of the DFT approach as implemented in the Quantum Espresso 6.5 package. The interacting system model, proposed for the computed electronic and geometrical structures of the BiOI modified with rGO, is composed of two layers of BiOI and one rGO layer as shown in Fig. 1. In the case of the rGO layer, an OH group and five epoxy groups were considered, which is in concordance with the experimental evidence for a C:O ratio of 2.23. In the interface model BiOI/rGO, the rGO was initially placed at 3 Å from BiOI and then optimized keeping the bottom layer of BiOI fixed. Since rGO and BiOI describe different crystal shapes, we fitted the nearest dimensions of each cell structure to build the combined supercell see Table 1.

Fig. 1 shows the different views and structures of BiOI(001) and rGO (001), employed in this study. The structure of BiOI(001) with the iodine layer exposed to rGO was selected, due to their superior stability both structurally and energetically compared with the oxygen-exposed

Table 1
Dimension parameters for cells of BiOI, rGO, and the final BiOI/rGO supercell.

Slab	a (Å)	b (Å)
BiOI(001) (2 × 1)	7.86	3.93
rGO(001) (c3x2)	7.40	4.26
BiOI/rGO	7.86	4.26

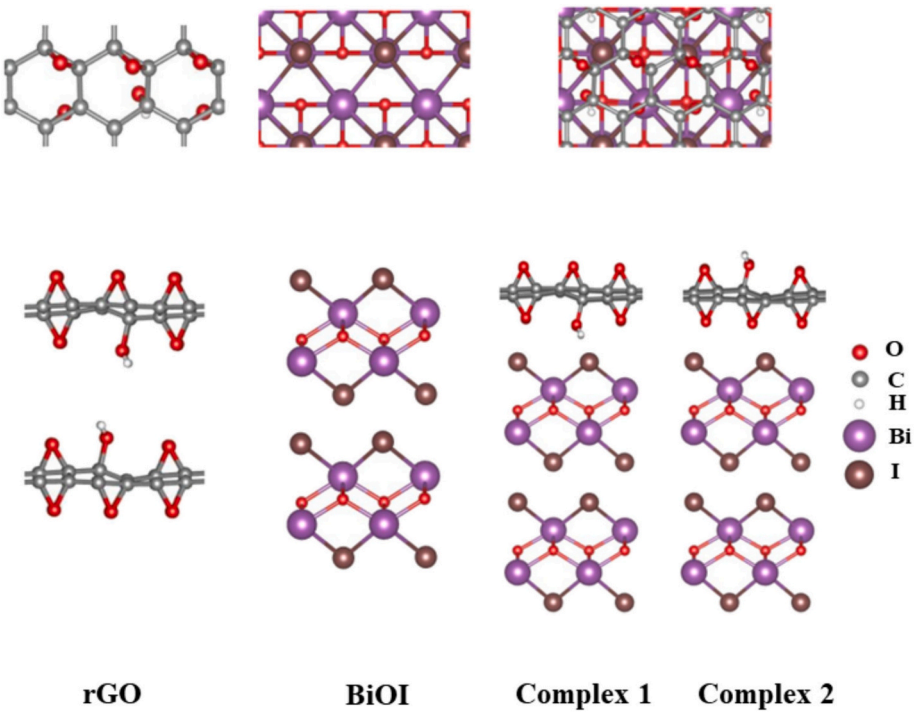

Fig. 1. Top view (top) and side view (bottom) of rGO, BiOI, and Complex 1 and Complex 2 (BiOI/rGO).

alternative. Two interaction models, as starting structures of the BiOI/rGO, were constructed depending on the orientation of the hydroxyl group attached to carbon 5 (C5) on the rGO layer, labeled as Complex 1 and Complex 2. The first complex (Complex 1) with the hydroxyl group facing directly toward the BiOI structure (**as** Fig. 1), while the other (Complex 2), displays the hydroxyl group oriented to the z-axis and opposed to BiOI.

Table 2 reports the distances of interface spacing between BiOI and rGO for Complex 1 and Complex 2 (in Å) and band properties (in electronvolts, eV). The results indicate that the final conformations of the BiOI/rGO material are structurally similar (despite the OH orientation) showing similar distances between BiOI and rGO, with 2.48 Å for complex 1 and 2.47 Å for complex 2.

Otherwise, DOS analysis shows that both complexes show improved performance of charge conduction, compared with their isolated counterparts. These results demonstrated that the band gaps (Eg) of BiOI decreased when rGO was incorporated, i.e. in the case of complex 1 and complex 2. Besides, when comparing both complexes, complex 2 shows slightly better conduction properties with shorter E_g than complex 1. Eg value from rGO varies in dependence on the oxygen content and their reduction [76] from 0.5 to 2.2 eV, which is in good agreement with our results. This phenomenon was shown in Table 2**,** where significant shifts in the valence band (E_{vb}) and a decrease in the band-gap (E_g) are observed.

It is worth noting that Eg value from rGO varies in dependence on the oxygen content and their reduction from 0.5 eV to 2.2 eV [76] and up to 2.96 eV depending on the experimental reduction method [https://doi.org/10.1016/j.apsusc.2020.145396]. For BiOI, experimental values of the band gap typically fall between 1.70 and 1.94 eV [77–79]. These ranges are in good agreement with our findings, presented in Table 2, where we obtained E_g values of 2.30 eV for rGO and 1.63 for BiOI, respectively. The slight underestimation of the band-gap energy in our calculations, compared with experimental values, can be attributed to the well-known limitations of the generalized gradient approximation (GGA) in accurately predicting band gaps m[81]In this sense, it is common to find in literature and many previous works, which have pointed out that DFT-calculated band-gaps suffer from underestimation regarding experimental measurements [31,80–82].

The PDOS of rGO and BiOI are illustrated (a) and (b) in Fig. 2, lines blue and red respectively. While the PDOS for heterostructures i.e. complex 1 and complex 2 are depicted in Fig. 2 **c, d** respectively, the total DOS of them are shown in the supplementary information section, **Figure SI2**. This analysis indicated that the interaction between rGO and BiOI allows the generation of the heterostructure BiOI/rGO. A relevant contribution of rGO states at the Fermi level is noted, which is given by a carbon atom, labeled as C(5) and shown as a green line in Fig. 2c. This carbon does not hold the hydroxyl or epoxy groups of the material/without being covalently bound to oxygen. This peak disappeared in the BiOI/rGO complex when the hydroxyl group was eliminated and only epoxy groups are present in the rGO. The PDOS for this system is reported in **Figure SI3.** This is consistent with the DOS analysis reported by [30], computed at the PBE and ultrasoft pseudopotential theoretical level, where the authors used the structural model for BiOI/rGO with only epoxide groups in the rGO sheet. Despite no transcendental differences were observed between complex 1 and complex 2 when we analyze PDOS, the assessment of the electron density differences provides very interesting results. Fig. 2 displays the electron density differences for both systems. Near the Fermi level, a distinct mixing of electronic states from rGO and BiOI is seen in both heterostructures studied, indicating the formation of mixed electronic states that may aid in interfacial charge transfer. This result is consistent with the change in the electronic states that contributes considerably to the top of the VB and the bottom of the CB, which has been previously discussed in studies like these of heterostructure formation [7,83]. Although they haven't specifically addressed the state mixing at the electronic level, other experimental studies have also documented improved charge separation and photocatalytic performance in BiOI/rGO composites, which is consistent with the existence of such interfacial coupling.

The analysis of electron density difference density evidences a distinct electronic behavior for both complexes, which is related to the orientation of the hydroxy groups of rGO at the interface BiOI/rGO. In the case of complex 1 when hydroxyl of rGO points toward the BiOI groups the electron density analysis shows a charge accumulation (red region) in I atoms and charge depletion on rGO represented by blue colour, see Fig. 3 a, evidencing interaction between these groups. On the other hand, complex 2, as observed in Fig. 3 **b**, shows charge depletion on I atoms and accumulation of charge on O atoms of rGO. These results suggest that charge transfer from BiOI to rGO can be most favored when the hydroxyl group is oriented opposite to the BiOI (complex 2). Also, that carbon atom (C5), describes a clear charge difference in the rGO, if the hydroxyl group is proximal or not to BiOI. This fact marks a difference compared with an rGO composed only of epoxide groups, as previously proposed by [30]. These results are consistent with a recent report finding that there is an electron transfer channel from BiOI to rGO in the structure of the composite, which favors the reduction of electron/hole recombination rates [84].

Frequencies analysis results show that the zone between 250 cm^{-1} and 400 cm^{-1} displays several signals, which are mainly oriented to rGO vibrational modes, oxygen layers of BiOI, and a mix of both. Considering that the unknown signal appears just for complexes, we compare resultant frequencies between interacting materials rGO/BiOI and their rGO and BiOI isolated geometries, allowing us to discard some common signals. Thus, analyzing just those signals that appear in the complexes. So, we can infer that the signal around 350 cm^{-1} could be attributed to the mix of rGO and oxygen vibrational modes of the BiOI, following this proposed model as shown in Fig. 4**.**

Discrete calculations of frontier orbitals show a remarkably small HOMO-LUMO gap (0.001 eV) in BiOI/rGO indicates exceptional electronic coupling between the components, facilitating efficient charge carrier migration across the interface. Although the band-gap values differ quantitatively from those reported in previous periodic calculations, this result is in concordance with the PDOS previously shown composition. In such composites, the HOMO and the LUMO reside on both the rGO sheets and the BiOI domains, creating directional electron transfer pathways visualized through spatial isosurface distributions (Fig. 5). The orientation of functional groups at the heterojunction critically modulates these electronic interactions - computational models reveal that hydroxyl group positioning on rGO significantly alters electron density distributions. When hydroxyl groups orient away from BiOI (Complex 2 configuration), charge accumulation occurs on oxygen atoms of rGO with corresponding depletion on iodine atoms in BiOI, optimizing electron transfer efficiency. This geometric dependence arises from the strong dipole interactions between rGO oxygen functionalities and BiOI halogen-terminated surface layers, which align the interfacial electric field to promote charge separation. The experimental results of Raman spectroscopy bellow confirm these interfacial interactions through the disappearance of Bi—I vibrational modes (85–149 cm^{-1}) and modified D/G band intensity ratios in the composite.

Table 2
Distance between BiOI and rGO in Å, and energetic parameters. All energy values in electronvolt (eV).

Complex	BiOI/rGO distance (Å)*	E_{vb} (eV)	E_{cb}(eV)	E_g(eV)
Complex 1	2.48	0.10	1.54	1.44
Complex 2	2.47	0.19	1.50	1.31
rGO	–	0.10	2.40	2.30
BiOI	–	0.05	1.68	1.63

* Calculated distance corresponds to the minimal distance between O(rGO) atoms and I atoms. E_{vb} is the energy of the valence band and E_{cb} is the energy of the conduction band calculated values with Eg value computed from the simulated system.

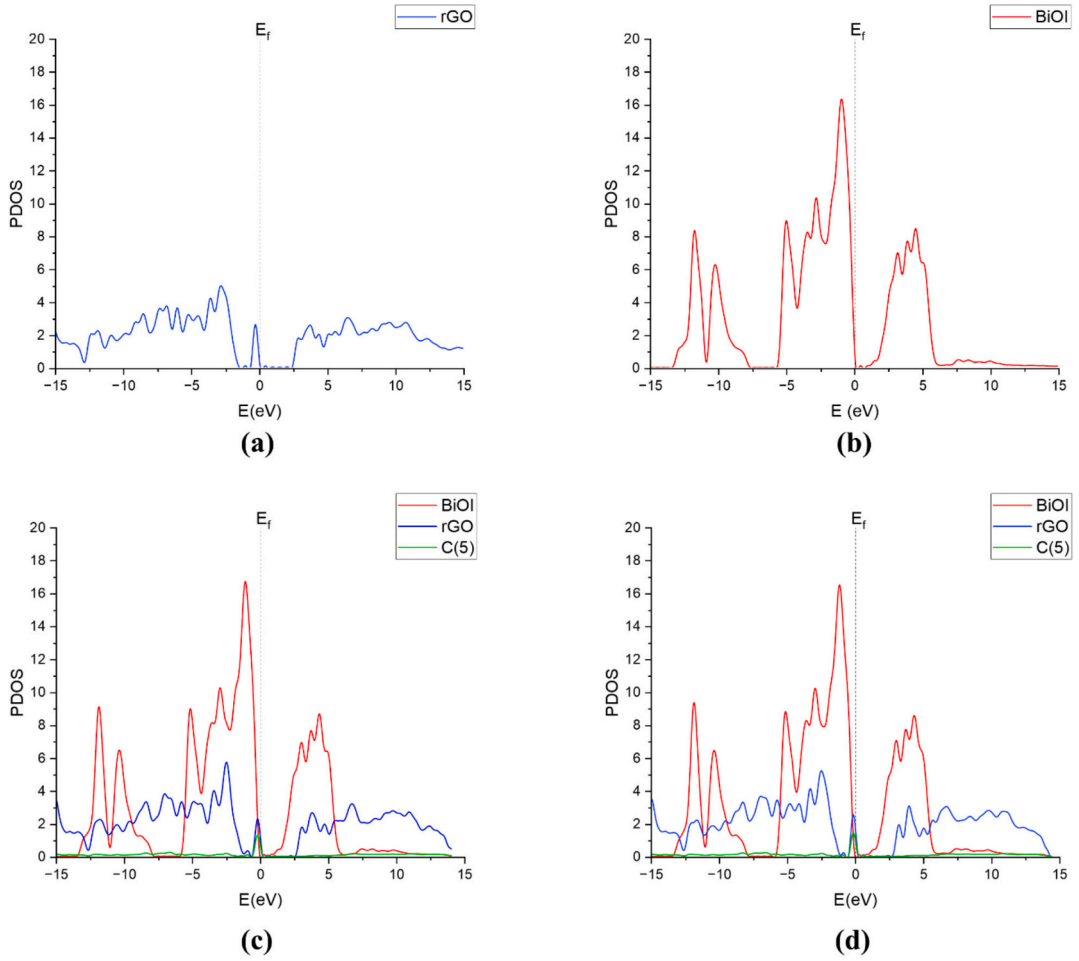

Fig. 2. Projected Density of States (PDOS) plots for isolated (a) rGO (blue) and (b) BiOI (red). PDOS plots of BiOI and rGO for (c) Complex 1 and (d) Complex 2. The Black dashed line represents the Fermi level (Ef). PDOS plots of Carbon atom (C5) are shown in green. Both complexes describe a coupling of states of BiOI and rGO at the Fermi level in line with the decrease of the band-gap and charge transfer. (For interpretation of the references to colour in this figure legend, the reader is referred to the web version of this article.)

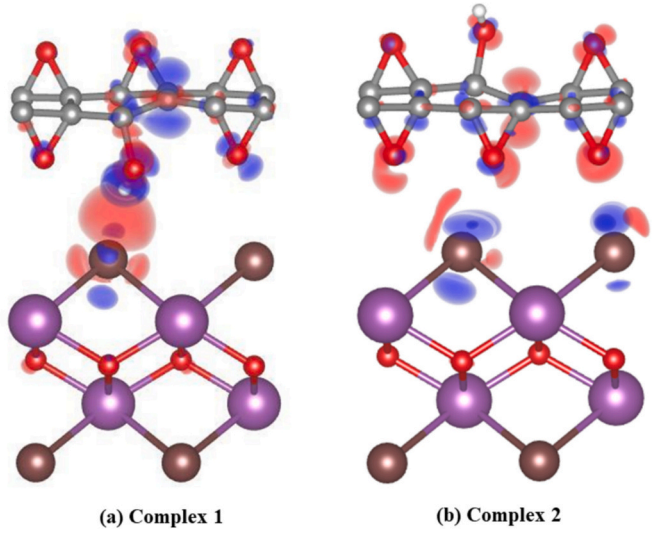

Fig. 3. The electron density difference between the two models BiOI/rGO. The Colour red describes the gain of electron density as complexes while blue means depletion of density (isovalue = 0.0005). (For interpretation of the references to colour in this figure legend, the reader is referred to the web version of this article.)

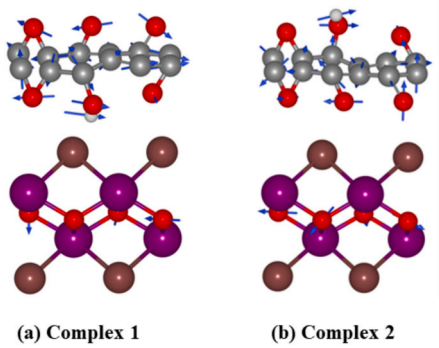

Fig. 4. Displacement vectors obtained for frequencies analyses for (a) Complex 1 (348.31 cm^{-1}) and Complex 2 (freq = 338 cm^{-1}).

The synergistic combination of rGO high carrier mobility and BiOI visible-light responsiveness creates a *Z*-scheme charge transfer mechanism, where photogenerated electrons in BiOI conduction band combine with holes from rGO valence band, preserving strong redox potentials for pollutant degradation. This electronic configuration, validated through density of states calculations, shows hybridized orbitals at the Fermi level that reduce recombination losses while maintaining sufficient overpotential for oxygen reduction and hydroxyl radical formation.

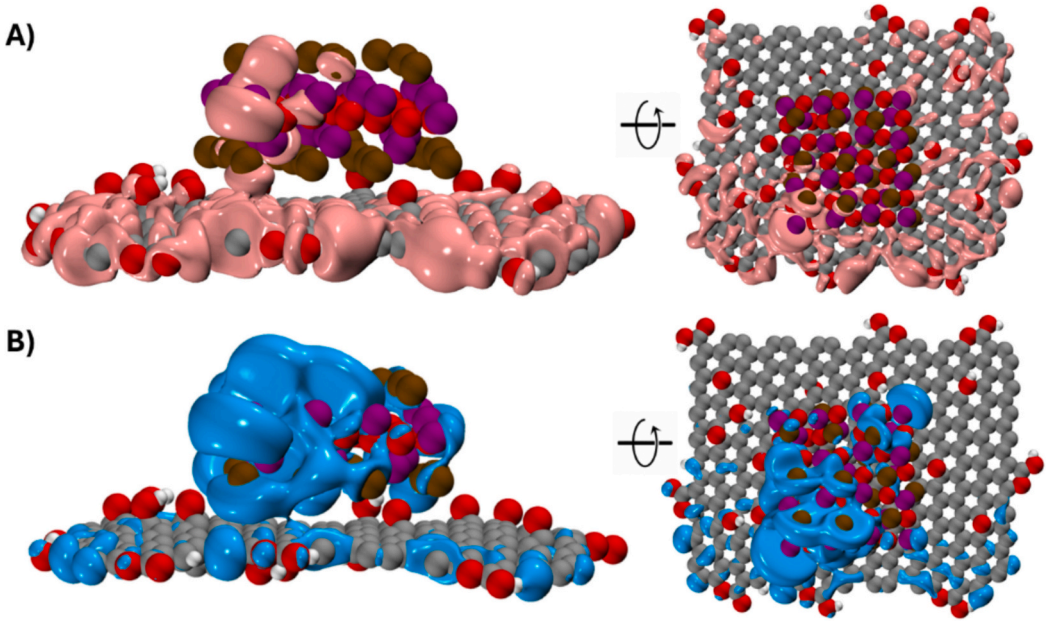

Fig. 5. Molecular orbital surface of A) LUMO and B) HOMO for BiOI/rGO complex obtained by GFN2-xTB method.

The topological analysis of BiOI/rGO interactions reveals critical insights into the electronic structure and bonding mechanisms at this heterojunction interface (Table 3 and Fig. 6-**B**). The bond critical point (BCP) data indicates three primary interaction types with distinct characteristics. The I—C interaction exhibits the lowest electron density ($\rho = 6.0 \times 10^{-3}$ a.u.) and negative potential energy density (V(r) = -3.5×10^{-3} a.u.), suggesting a weak but stable interaction. The I—O interaction shows moderately higher electron density ($\rho = 7.5 \times 10^{-3}$ a.u.) and more negative potential energy (V(r) = -4.8×10^{-3} a.u.), indicating stronger halogen bonding. Most notably, the Bi—O interaction demonstrates significantly higher electron density ($\rho = 1.7 \times 10^{-2}$ a.u.) and the most negative potential energy (V(r) = -1.3×10^{-2} a.u.), confirming it as the strongest interaction at the interface. All interactions display positive Laplacian values ($\nabla^2\rho > 0$) and positive total energy density (H(r) > 0), characteristic of closed-shell interactions rather than covalent bonds. A complete description of all interactions can be found in the supplementary material **Table SI1**.

The IGMH analysis complements these findings by visualizing the spatial distribution and strength of non-covalent interactions. The isosurfaces in Fig. 6-**A** clearly differentiate between weak van der Waals forces (green regions) dominating the I—C interactions and stronger halogen bonding (blue regions) occurring between iodine and oxygen atoms, particularly with the hydroxyl groups on the rGO surface. This colour-coded visualization aligns with the quantitative δg values from the topological analysis, where Bi—O interactions show the highest δg (3.5×10^{-2} a.u.), followed by I—O (1.5×10^{-2} a.u.) and I—C (1.0×10^{-2} a.u.). The AIM molecular graph in Fig. 6-**B** further confirms these findings by revealing bond paths and critical points that map the electron density topology. The presence of (3,+1) and (3,−1) critical points indicate ring and cage structures forming at the interface, while the (3,+3) critical points mark local minimum in the electron density. The strong Bi—O interactions create efficient charge transfer pathways across the interface, while the network of weaker I—C and I—O interactions stabilize the overall structure and maintain optimal separation between the components, preventing aggregation while enabling electronic coupling.

Table 3
Average topological analysis of the bonding critical points (BCP) of BiOI/rGO complex. Electron density (ρ), Potential energy density V(r), Total energy density H(r), Laplacian of electron density ($\nabla^2\rho$), Lagrangian kinetic energy G(r), sign(λ^2)ρ, and δg function. All values are given in atomic units (a.u.).

Bonds	ρ	V(r)	H(r)	$\nabla^2\rho$	G(r)	sign $(\lambda^2)\rho$	δg
BiOI/rGO							
I–C	6.0×10^{-3}	-3.5×10^{-3}	2.1×10^{-3}	3.1×10^{-2}	5.6×10^{-3}	-6.0×10^{-3}	1.0×10^{-2}
I–O	7.5×10^{-3}	-4.8×10^{-3}	2.4×10^{-3}	3.9×10^{-2}	7.2×10^{-3}	-7.5×10^{-3}	1.5×10^{-2}
Bi–O	1.7×10^{-2}	-1.3×10^{-2}	2.4×10^{-3}	7.8×10^{-2}	1.5×10^{-2}	-1.7×10^{-2}	3.5×10^{-2}

The tight-binding molecular dynamic simulations reveal remarkable kinetic stability in the BiOI/rGO heterostructure, where the BiOI cluster maintains consistent interfacial contact with the rGO surface throughout the simulation trajectory (Fig. 7). This stability is facilitated by multiple non-covalent interactions that develop and persist during the computational experiment. The simulation demonstrates excellent convergence over time, with complementary Root Mean Square Deviation (RMSD) analysis in **Figure SI4** and **VideoSI1** showing minimal structural fluctuations-all values remaining below 1 Å relative to the 30 ps reference structure, indicating a well-equilibrated system with limited conformational changes. Particularly noteworthy is the pronounced interaction between iodine atoms and the oxygen-containing functional groups on the rGO surface, especially the hydroxyl moieties, which form halogen bonds with electron densities in the range of 7.5×10^{-3} a.u. and potential energy densities of -4.8×10^{-3} a.u. These I—O interactions create a network of stabilizing forces that anchor the BiOI cluster to specific sites on the rGO surface. Additionally, the aromatic carbon rings of rGO establish weaker but significant interactions with the BiOI cluster (electron density 6.0×10^{-3} a.u.), contributing to the overall interfacial stability through π-halogen contacts. The positive Laplacian values ($\nabla^2\rho > 0$) observed for all interactions confirm their closed-shell nature, consistent with the non-covalent character expected at such interfaces. This stable configuration enables efficient charge transfer across the BiOI/rGO interface, explaining the potential enhanced photocatalytic performance under visible light irradiation.

3.2. Experimental results

3.2.1. Structural analysis

Fig. 8 displays the XRD patterns of as-synthesized samples obtained

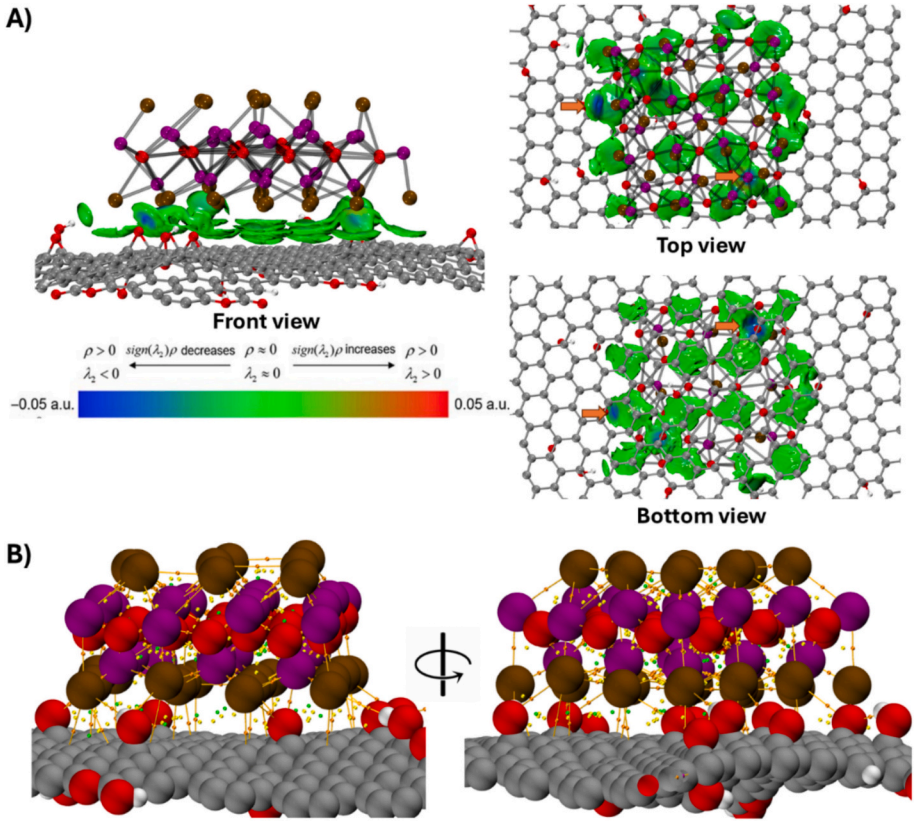

Fig. 6. A) IGMH analysis ($\delta g^{inter} = 0.001$ a.u.) and B) AIM molecular graph showing the different BCPs for BiOI/rGO complex. Green, yellow, and orange spheres in the above map correspond to (3,+3), (3,+1), and (3,−1) critical points, respectively. Brown lines denote bond paths. (For interpretation of the references to colour in this figure legend, the reader is referred to the web version of this article.)

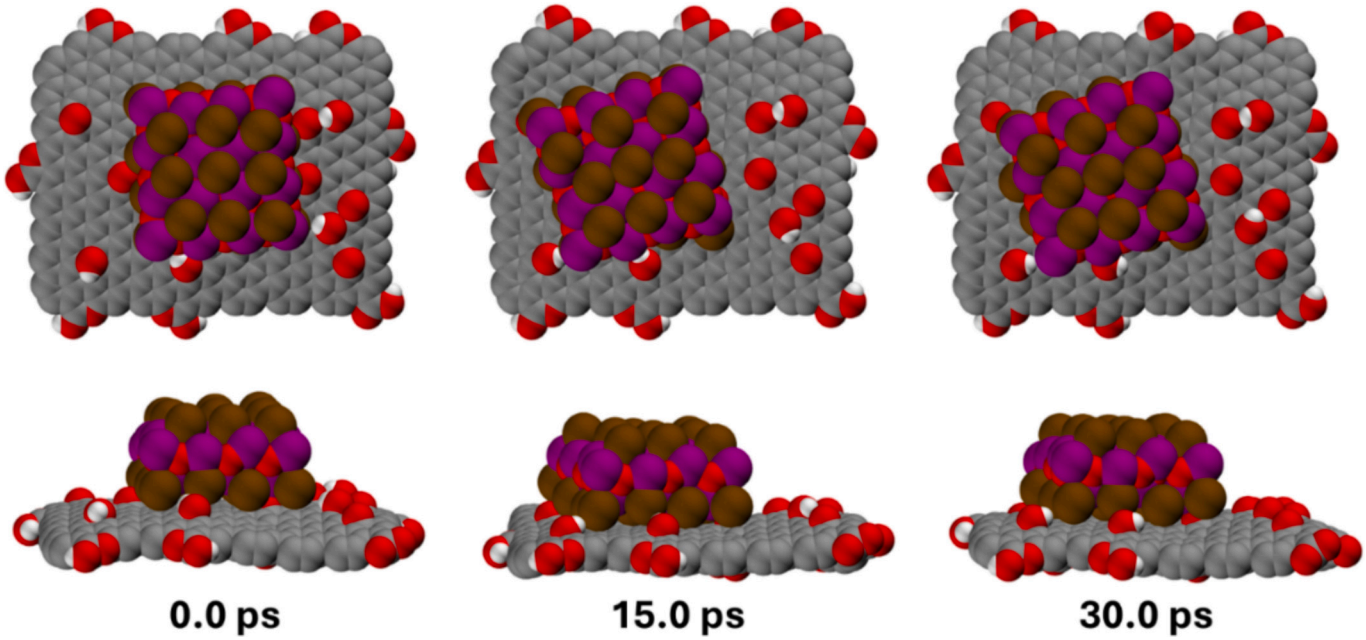

Fig. 7. Sequential snapshots demonstrating BiOI interaction with rGO surface, illustrating initial (0 ps) placement and final (30 ns).

for 2Θ values from 5 to 80°. XRD pattern of BiOI showed the main peaks at 2θ: 9.66°, 29.66°, 31.65° 45.37°, 51.34° and 55,13° that corresponds to (001), (012), (110), (020), (114) and (122) planes. All peak corresponds to the tetragonal P4/nmm (129) crystal phase BiOI possesses a Sillen structure, that is composed of $[Bi_2O_2]^{2+}$ layers with I ions between them. The lattice constant obtained from Rietveld refinement was (a = b = 4.02 Å and c = 9.04 Å) agree with the standard values (a = b = 3.995 Å and c = 9.15 Å), as can be seen in Table 1 and correspond to Reference code: 98–039-1354. The most significant highest intensity of distinctive peaks corresponds to (012) and (110) crystal facets. As denoted in the

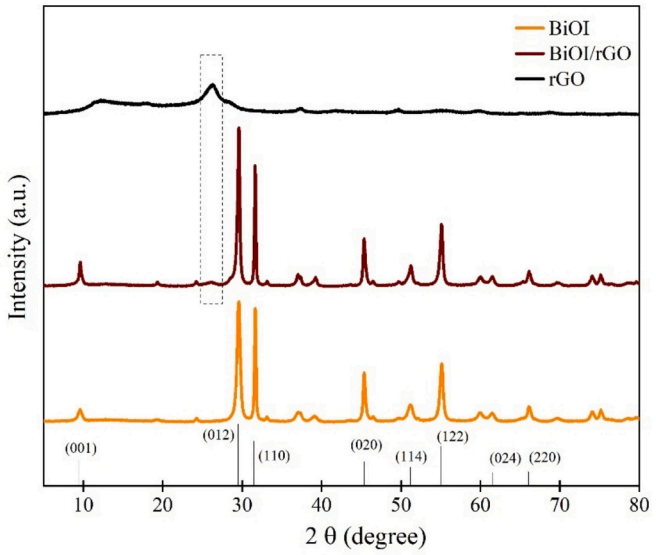

Fig. 8. XRD patterns for as-synthesized samples of rGO, BiOI/rGO, and BiOI. The colour was obtained as a function of rGO content.

dotted box, an additional a (003) diffraction peak was found attributable to the reduction of graphene [85]. In the case of BiOI/rGO material due to relatively low amounts of rGO, the (003) diffraction peaks were hardly detected.

We note that the intensity of the peak of 9.6 (001) in the BiOI/rGO increases more than BiOI pure material suggested by rGO addition. This phenomenon indicates that in the synthesis process, the addition of rGO plays an important role in the conversion and formation of (001) faceted crystal structure. Also, the increased crystallite size of the BiOI/rGO crystals compared to BiOI pure shown in Table 1, suggests a strong influence of rGO on the crystal structure of BiOI. Using representative slabs of the planes (012) and (110), for BiOI/rGO, the oxygen-rich (012) and (110) planes grew parallel to the substrate plane due to the tendency of graphene to physically adsorb O_2 molecules into its surface, effectively making it a nucleation site for the growth of the (110) and (012) planes [86]. No characteristic peaks from other phases are detected, thus indicating the formation of highly pure products. Moreover, in the XRD spectra, the width at half the maximum (FWHM) decreases, indicating a further increase in the size of the BiOI/rGO crystals compared to pure BiOI. The interlayer spacing calculated for rGO was 3.39 Å, which was more than but quite close to the standard (3.40 Å) or commercial graphite (3.35 Å) interlayer spacing [87]. All values for lattice parameters, interplanar spacing, and crystallite size are listed in Table 4.

3.2.2. SEM, TEM, and EDS

Fig. 9 shows the SEM, and TEM image analysis obtained for all as-synthetized materials. The SEM images of rGO (Fig. 9a) while BiOI pure (Fig. 9b) present many hierarchical microspheres, as well as some irregular nanosheets distributed among them. In the case of BiOI/rGO, (Fig. 9c) the microspheres show no obvious differences between the edges and centers. It is very important to note that the 3D microstructures that showed in several studies have great activity and photodegradation [6,88,89]. The BiOI and BiOI/rGO samples are made up of agglomerate microspheres with an average diameter ranging from ~0.5 to 2.0 μm. Meanwhile, the TEM image of the rGO sheet is displayed in Fig. 9d, rGO was a transparent 2D sheet with several folds, which resulted in a broad diffraction pattern (Fig. 8) that resembles the few and multi-layered graphene sheets [90]. In pure BiOI (Fig. 9e), cubic structures or crystals with generally small dimensions are observed. In contrast, in BiOI/rGO (Fig. 9f), the presence of BiOI on the surface of the rGO sheets is evident, suggesting an interaction between the two materials. Additionally, the presence of Bi, O, I, and C elements in the samples was evidenced by EDS analysis as indicated in **Figure SI5.**

3.2.3. N_2 adsorption-desorption isotherms

The specific surface areas (A_{BET}) and porosity of the BiOI/rGO, BiOI, rGO, and TiO_2 architectures were investigated by N_2 adsorption and desorption isotherms. Fig. 10 shows the isotherms for each material. The BiOI/rGO and BiOI are non-porous materials that tend not to close the hysteresis cycles. The pore size distribution curves range from 6.16 to 7.09 nm. The presence of mesoporous suggests an improvement in the catalytic activity of the products by allowing easy penetration of light waves [91]. The A_{BET} obtained was very small, with values of 16, 8, 6, and 47 m^2g^{-1} for rGO, BiOI/rGO, BiOI, and TiO_2, respectively (see Table 5). It can be noted that the surface area of BiOI/rGO only increased slightly in comparison with the BiOI pure. The as-synthetized samples exhibited an A_{BET} minor than the values reported in previous studies [6,92]. Thus, the effect of A_{BET} on the changes in the photocatalytic activities of BiOI/rGO and BiOI can be neglected.

3.2.4. UV–visible diffuse reflectance spectra

To determine the effect of the incorporation of graphene on the light absorption of BiOI, UV–Visible diffuse reflectance spectra (DRS) were used. Figs. 11 **a, b** shows the DRS for each material. The absorption spectrum of samples in **Fig. 11**a shows significant variation if compared with TiO_2 Degussa P25. The absorption edges of TiO_2, BiOI, and BiOI/rGO were 430 nm, 656 nm, and 750 nm, respectively. This absorption band maximum is nominally shifted to a lower wavelength in the case of the BiOI/rGO. It was found that the band-gap decreases when rGO is added to the pure material from 1.91 to 1.82 eV. Similar results have been reported in previous works by [7]. These results also reveal that the rGO addition reduces the band-gap. In this sense, the material can be activated by solar radiation which would mean great energy-saving since ~55 % corresponds to the visible range of the total energy emitted by the Sun [93]. The E_{vb} of the materials (BiOI/rGO and BiOI) are more positive than the standard redox potentials of $^{\circ}OH/OH^{-}$ (1.99 eV), H_2O_2 (1.77 eV), and O_3 (2.07 eV), indicating that such materials may have much stronger oxidation abilities. The E_{vb} value of BiOI/rGO is more positive than the redox potential of MO (1.48 eV versus NHE).

Table 4
Lattice parameters, interplanar spacing, full width at half maximum, and crystallite size were measured for samples.

Sample	a = b (Å)	c (Å)	d (Å)				FWHM				D (nm)
			(001)	(012)	(110)	(003)	(001)	(012)	(110)	(003)	BiOI
rGO	2.208	10.195	–	–	–	3.390	–	–	–	0.981	–
BiOI/rGO	4.005	9.237	9.237	3.028	2.832	3.426	0.313	0.334	0.200	0.020	23.37
BiOI	3.994	9.198	9.237	3.028	2.832	–	0.644	0.486	0.224	–	17.93
Standard of BiOI 98–039-1354	3.995	9.151	9.151	3.009	2.825	–	–	–	–	–	
Standard of rGO 98–005-3780	2.516	10.209	–	–	–	3.403	–	–	–	–	–

The interlayer distance (d) is calculated using the Bragg equation
Crystallite size (D) from XRD using the Scherrer equation, FWHM (full width at half maximum)

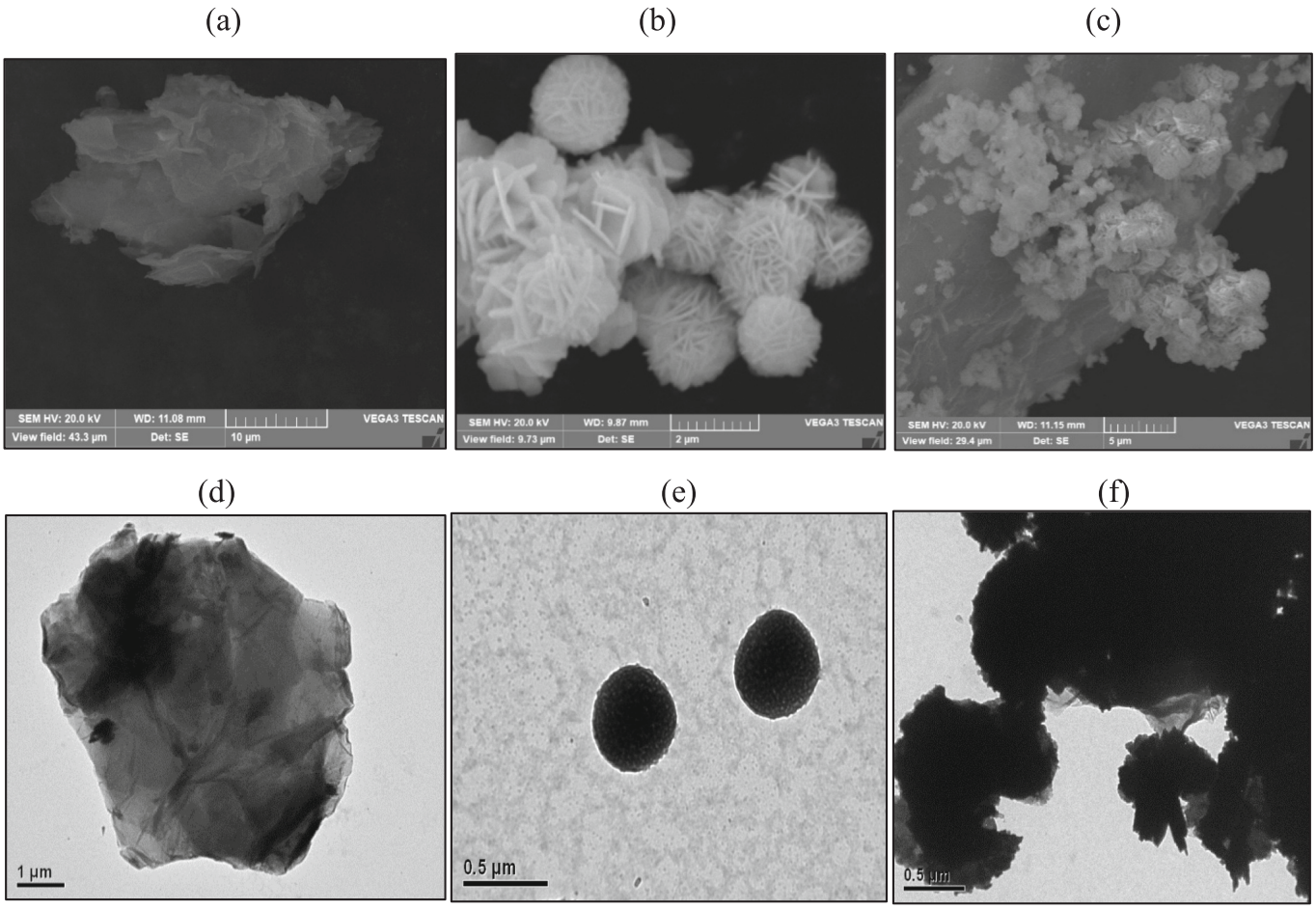

Fig. 9. SEM (above), and TEM (below) analysis of (a) rGO sheet, (b) BiOI pure, and (c) BiOI/rGO material.

Therefore, the photogenerated holes can oxidize the MO directly. Eg the value from rGO, varies in dependence on the oxygen content and their reduction, [76] from 0.5 to 2.2 eV, which agrees with our results.

Table 5 shows the structural and electronic properties of the photocatalysts. We appreciate that the structure of BiOI does not change with the addition of the rGO. The only thing that changes significantly is the band gap.

3.2.5. *Raman analysis*

For additional exploration, Raman spectroscopy was carried out for the samples. Raman spectroscopy is a powerful technique for the characterization of sp^2 and sp^3 hybridized carbon atoms that are contained in graphene. Fig. 12 showed that the BiOI exhibits two intense peaks at 85 and 149 cm^{-1} which are assigned to the A_{1g} and Eg stretching modes of Bi—I bonds respectively [94]. These bands below 200 cm^{-1} are halogen sensitive and are assigned to modes involving the motion of the halogen atoms [95]. The peak between 300 and 600 cm^{-1} is due to the change in the Bi—O environment [96] suggested by the composite formation. When the BiOI covalently interacts with the graphene, the crystal symmetry changes, and therefore the A_{1g} and Eg bands disappear (**inset** Fig. 12). G-band at around 1576 cm^{-1}, due to interphase vibration of the graphite lattice and first-order scattering of the E_{2g} mode [97]. D band is common for disordered sp2 carbon, the BiOI/rGO sample exhibits less intense peaks compared with the pure rGO sample, which indicates a decreased crystallinity during the formation of the BiOI/rGO [98]. The intensity and broadness of the 2D band in graphene are a function of the number of layers [97]. In this study, 2D band shows low intensity suggesting that BiOI/rGO has a low number of graphene layers. The peak positions of G and D bands in the BiOI/rGO spectrum, regarding the rGO sample, is indicative of the formation of the composite. Also, the D + G band is a combination band related to the concentration of defects due to the present oxygenated groups [99].

3.2.6. *Testing the photocatalytic properties*

It was confirmed that the concentration of MO doesn't change under dark conditions and visible artificial light irradiation without catalysts for 4 h. Hence, in our experiment, dye degradation occurs in the adsorption and photocatalytic process. The photocatalytic activities of as-synthetized samples are shown on Fig. 13**.** The enhanced PE of BiOI increases when rGO is added, suggested by the change in exposure on the reactive faces of BiOI/rGO (001) and decreases the Eg (Figs. 8, 11**)**. Highly reactive facets can effectively enhance surface properties and improve the separation of photo-generated carriers [17], decreasing the rapid recombination of electron-hole pairs and therefore the PE increases. Also, the minor Eg (1.91 eV, in BiOI/rGO) could favor easier production of active species, making the photocatalytic process more efficient. rGO improves the morphology, stability, and surface accessibility of BiOI. Thus, their combination prevents nanoparticle aggregation, leading to better dispersion and more exposed active sites. Furthermore, their combination helps to electron displacement process. In this sense, the photoactivity of the composite was 2.5 times higher than pristine BiOI. The A_{BET} of BiOI/rGO (8 $m^2\ g^{-1}$) was slightly more than BiOI (6 $m^2\ g^{-1}$), and when compared with standard TiO_2 P25 (47 $m^2\ g^{-1}$), the BiOI/rGO shows a photocatalytic efficiency like standard TiO_2. Therefore, we suggested that the main factors for the enhancement of PE in the composite were changes in Eg, the orientation of the hydroxyl group, more exposure to the reactive facets, and decreased electrostatic interaction since at working pH both the substrate and the

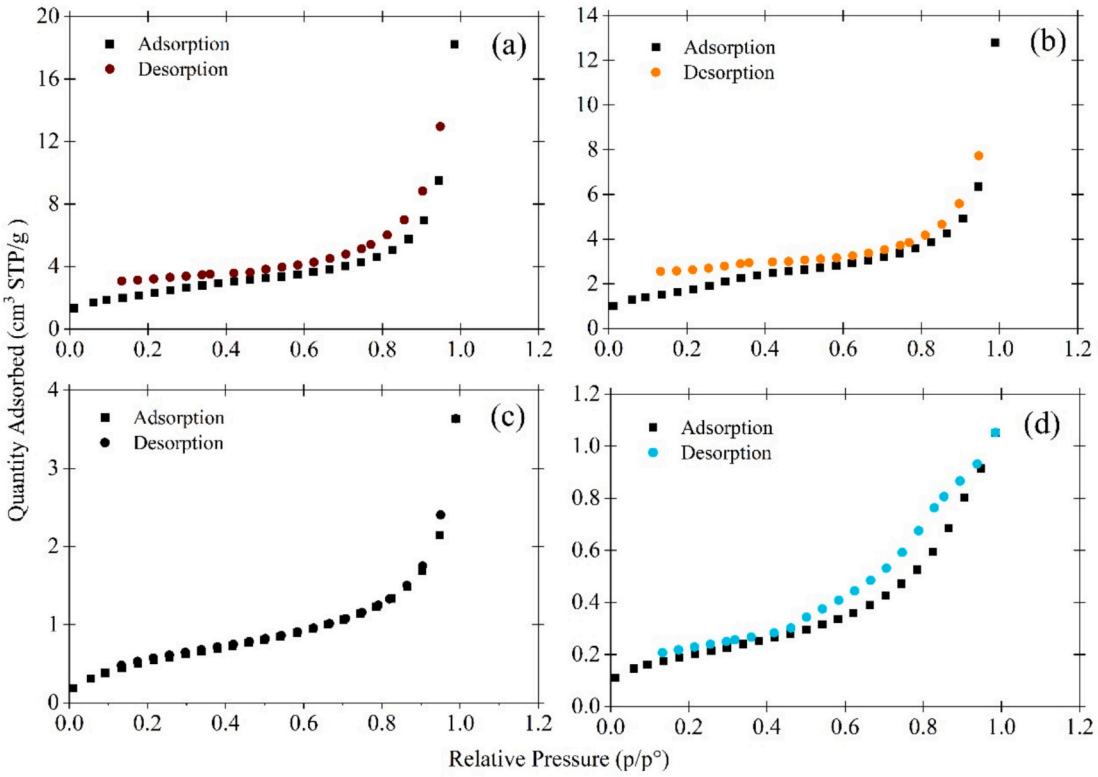

Fig. 10. N_2 adsorption-desorption isotherms for (a) BiOI/rGO, (b) BiOI pure, (c) rGO and (d) TiO_2 samples.

Table 5
Summarized structural and electronic properties of the as-synthesized samples.

Materials		Crystallite size[a] (nm)	S_{BET} (m^2g^{-1})	Pore size (nm)	Pore volume ($cm^3\ g^{-1}$)	Band-gap[b]	E_{vb}	E_{cb}
	TiO_2	BiOI				(eV)		
BiOI/rGO		23.37	8	7.09	0.02	1.82	2.35	0.53
BiOI		17.93	6	6.16	0.01	1.91	2.39	0.48
rGO		–	16	7.88	0.03	0.52	1.76	1.24
TiO_2 P25	21*	–	47	6.31	0.07	3.00	2.80	0.20

[a] Calculated from XRD measurements using the Scherrer equation.
[b] Calculated from the diffuse reflectance UV–vis spectra using the Kubelka–Munk function.
* Take from [91].

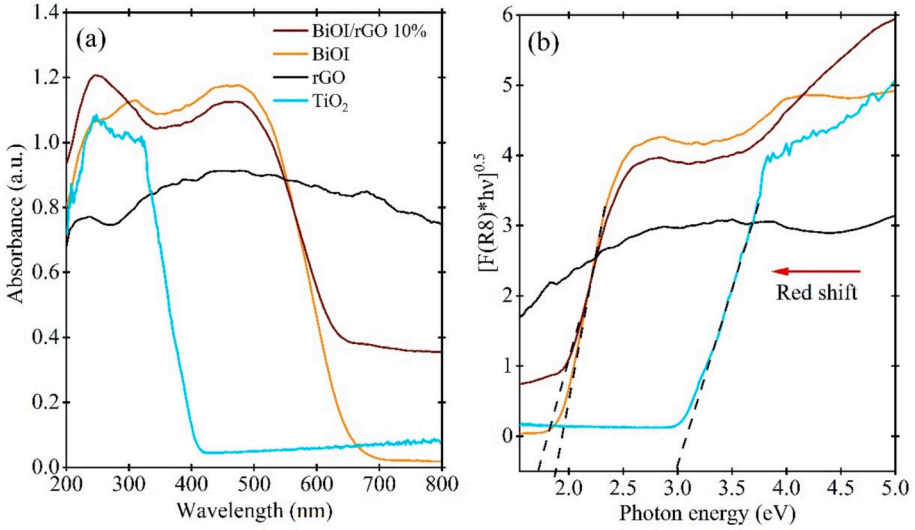

Fig. 11. (a) UV–vis diffuse reflectance spectra for as-synthesized samples.

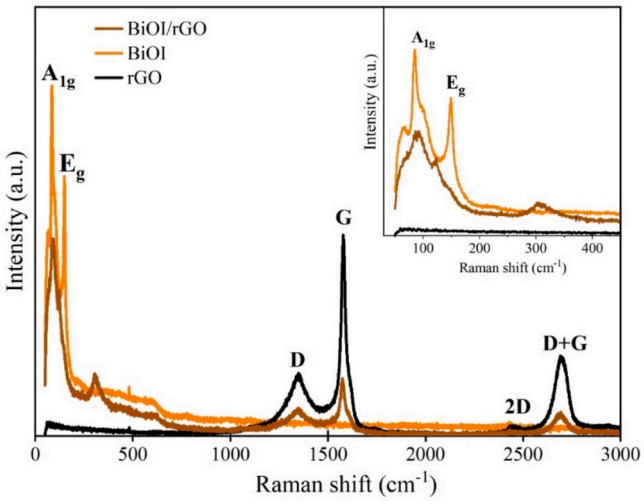

Fig. 12. Raman analysis of as-synthesized samples of rGO, BiOI and BiOI/rGO. Inset, was zoomed between 100 and 450 cm^{-1} Raman bands.

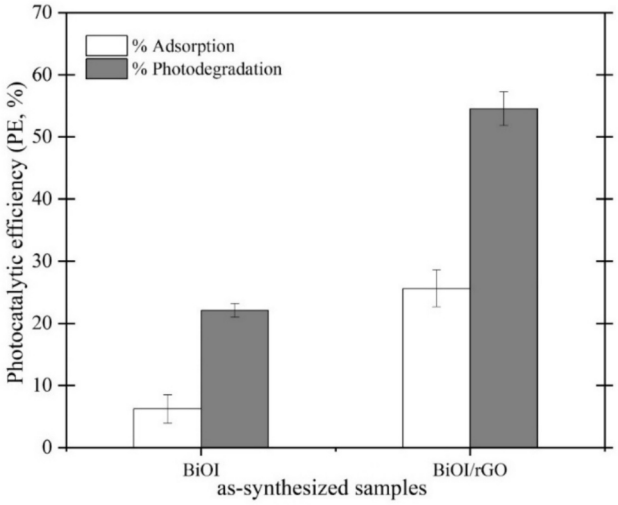

Fig. 13. Photocatalytic activity of as-synthesized samples on the degradation of MO under simulated visible light irradiation using 41.9 umol/L (MO) and 30 mg (as-synthesized samples) during 120 min.

BiOI/rGO are negative. Several methods have been reported for the synthesis of BiOI-based materials [24,27,100,101]. But most of them are complex, used at high temperatures, not environmentally benign, and recognized with high costs, e.g., when used in ionic liquids [66,102], or expensive reagents [24]. However, the reflux method developed here shows great advantages, the process is developed at low temperatures, without the presence of surfactants, stable agents, or ionic liquids which greatly reduces costs. The reagents, solvents and reflux conditions are well suited for any scale up process with minimal efforts.

Table 6 shows a comparative photocatalytic performance analysis of BiOI/rGO composite with similar photocatalysts reported in previous literature. Although our material requires improvement, by optimizing the amount of rGO, it provides efficiencies as those reported in the literature. It is asserted that the BiOI/rGO photocatalyst is a promising material with which to develop new technologies in the field of wastewater treatment, as well as for the degradation of organic pollutants and the creation of antibacterial and antiviral surfaces [5–8], [103]. Additionally, it can be used as a sensor, among other applications [104].

Table 6
Comparison of the degradation rate of organic pollutants with previously published results under visible light irradiation.

Photocatalyst	Pollutant	Photocatalytic Performance	Notes	Refs.
BiOI/rGO	MO	~2.5 times higher photocatalytic activity than pristine BiOI	Efficient degradation but, limitation in optimizing the amount of rGO	**This study**
rGO-BiOI	MO	4.2 times higher photocatalytic activity than pristine BiOI	Better results optimizing the amount rGO. The best material was rGO1/400–BiOI	[7]
C-BiOI	MO	4.4 times higher photocatalytic activity than pristine BiOI	Better results optimizing the carbon doped. The best material was C-BiOI-2	[8]
BiOI/rGO composite	4-Fluoroaniline degradation	~2.5 times higher photocatalytic activity than pristine BiOI; >99 % degradation efficiency	Efficient degradation and high stability, enhanced charge separation due to rGO hybridization	[9]
BiVO4/rGO	Methylene Blue dye	2 times higher degradation rate than pure BiVO4	Enhanced specific surface area and charge separation; pseudofirst-order rate constant doubled	[10]
N-TiO_2/BiOI/rGO	Methylene Blue dye	99.22 % MB degradation in 60 min under sunlight; significantly higher than TiO_2, BiOI, and binary composites	Composite with specific surface area 139.56 m^2 g^{-1} and bandgap ~1.24 eV; excellent visible-light response	[11]
$BiFeO_3$/rGO Composites	Methylene Blue dye	2.7 times than that of $BiFeO_3$	Optimizing the rGO doped. The best material was BGO60	[105]
BiOCl–rGO	Rhodamine B dye	Better photocatalytic activity than pure BiOCl	Size-controlled composites with PVP surfactant enhancing degradation efficiency	[25]

4. Conclusions

BiOI and BiOI/rGO were successfully synthesized via a facile, and cheap method. Using different experimental and theoretical techniques including X-ray diffraction, N_2 adsorption-desorption isotherms, SEM, TEM, Raman, DRS, and density functional theory calculations (DFT) the materials were studied. The results indicated that BiOI/rGO has a crystal structure considerably stable, where crystallite size and the lattice parameters experienced only slight changes. It was also demonstrated that the rGO in the BiOI system played an essential role. Experimental and theoretical results show that electronic interaction between rGO sheet and BiOI reduced the band-gap, with good DFT approximated band-gap values. The interfacial charge transfer was analyzed via electron density difference based on two interaction models, taking into account the orientation of the hydroxyl group attached to carbon number 5 on rGO. This analysis showed the role of the hydroxyl group and epoxy groups in

the charge transfer along the interfacial direction of heterostructure BiOI/rGO. The tight-binding molecular dynamic simulations reveal remarkable kinetic stability in the BiOI/rGO heterostructure, where the BiOI cluster maintains consistent interfacial contact with the rGO surface throughout the simulation trajectory. The photocatalytic testing indicates that BiOI/rGO is 2.5 times higher than its counterpart of BiOI pure. BiOI/rGO is a candidate excellent for organic dye degradation under UV–vis irradiation and warrants further investigations toward promising applications in solar energy and chemistry, to use visible light more efficiently. The material will provide a novel strategy to facilitate the treatment of polluted waters in environmental engineering.

CRediT authorship contribution statement

Lisdelys González-Rodríguez: Writing – review & editing, Writing – original draft, Visualization, Validation, Supervision, Software, Resources, Project administration, Methodology, Investigation, Funding acquisition, Formal analysis, Data curation, Conceptualization. **Osvaldo Yañez:** Writing – review & editing, Writing – original draft, Visualization, Validation, Supervision, Software, Resources, Project administration, Methodology, Investigation, Funding acquisition, Formal analysis, Data curation. **David Contreras:** Writing – review & editing, Validation, Supervision, Methodology, Investigation, Formal analysis. **Yoan Hidalgo-Rosa:** Writing – review & editing, Writing – original draft, Visualization, Validation, Supervision, Software, Methodology, Investigation, Formal analysis, Data curation. **Ximena Zarate:** Writing – review & editing, Visualization, Supervision, Software, Investigation, Formal analysis, Data curation, Conceptualization. **Mario Saavedra-Torres:** Writing – review & editing, Visualization, Validation, Software, Methodology, Formal analysis, Data curation. **Eduardo Schott:** Writing – review & editing, Validation, Supervision, Methodology, Investigation, Formal analysis, Conceptualization. **Carolina Baeza:** Writing – review & editing, Writing – original draft, Visualization, Validation, Methodology, Investigation, Formal analysis, Conceptualization. **Udayabhaskar Rednam:** Writing – review & editing, Writing – original draft, Visualization, Validation, Methodology, Investigation, Formal analysis, Data curation, Conceptualization. **R.V. Mangalaraja:** Writing – review & editing, Methodology, Conceptualization. **Daniel Mondaca:** Writing – review & editing, Writing – original draft, Visualization, Validation, Methodology, Formal analysis, Data curation, Conceptualization.

Declaration of competing interest

The authors declare that they have no known competing financial interests or personal relationships that could have appeared to influence the work reported in this paper.

Acknowledgments

L. G-R thanks the competitive Fund for Regular Research Projects 2023-2025 granted by Universidad de Las Américas (UDLA). Also acknowledge to Boris Friedman, Apogee Distributor - Technologies Omega Ltd. The National Agency for Research and Development (ANID, Chile) through FONDECYT project 1251871. Powered@NLHPC: This research was partially supported by the supercomputing infrastructure of the NLHPC (CCSS210001). ANID/FONDAP/ 1523A0006. Y·H-R is grateful for the ANID Postdoctoral 3230141. FONDECYT 1241917.

Appendix A. Supplementary data

Supplementary data to this article can be found online at https://doi.org/10.1016/j.rechem.2025.102706.

Data availability

Data will be made available on request.

References

[1] D. Contreras, V. Melin, G. Pérez-González, A. Henríquez, L. González, Advances and Challenges in BiOX (X: Cl, Br, I)-Based Materials for Harvesting Sunlight, 2020, https://doi.org/10.1007/978-3-030-15608-4_10.
[2] G.J. Lee, Y.C. Zheng, J.J. Wu, Fabrication of hierarchical bismuth oxyhalides (BiOX, X = cl, Br, I) materials and application of photocatalytic hydrogen production from water splitting, Catal. Today 307 (2018) 197–204, https://doi.org/10.1016/j.cattod.2017.04.044.
[3] D.S. Bhachu, S.J.A. Moniz, S. Sathasivam, D.O. Scanlon, A. Walsh, S.M. Bawaked, M. Mokhtar, A.Y. Obaid, I.P. Parkin, J. Tang, C.J. Carmalt, Bismuth oxyhalides: synthesis, structure and photoelectrochemical activity, Chem. Sci. 7 (2016) 4832–4841, https://doi.org/10.1039/C6SC00389C.
[4] J. Di, J. Xia, H. Li, S. Guo, S. Dai, Bismuth oxyhalide layered materials for energy and environmental applications, Nano Energy 41 (2017) 172–192, https://doi.org/10.1016/j.nanoen.2017.09.008.
[5] B., D.T.K., K.M., S.P, K.M. Toroń, Impact of hydrochloric acid doping on polyaniline conductivity and piezoelectric performance in polyaniline/bismuth oxyiodide nanocomposites, Compos B Eng 289 (2025).
[6] J.C. Durán-Álvarez, C. Martínez, A.C. Mera, R. Del Angel, N.J. Gutiérrez-Moreno, R. Zanella, A facile synthetic method to obtain bismuth Oxyiodide microspheres highly functional for the photocatalytic processes of water depuration, J. Vis. Exp. (2019), https://doi.org/10.3791/59006.
[7] X. Ren, J. Yao, L. Cai, J. Li, X. Cao, Y. Zhang, B. Wang, Y. Wei, Band gap engineering of BiOI: via oxygen vacancies induced by graphene for improved photocatalysis, New J. Chem. 43 (2019) 1523–1530, https://doi.org/10.1039/c8nj05538f.
[8] L. Zeng, F. Zhe, Y. Wang, Q. Zhang, X. Zhao, X. Hu, Y. Wu, Y. He, Preparation of interstitial carbon doped BiOI for enhanced performance in photocatalytic nitrogen fixation and methyl orange degradation, J. Colloid Interface Sci. 539 (2019) 563–574, https://doi.org/10.1016/j.jcis.2018.12.101.
[9] C. Lv, H. Cheng, R. Fan, J. Sun, X. Liu, Y. Ji, Fabrication of rGO/BiOI photocathode and its catalytic performance in the degradation of 4-Fluoroaniline, Heliyon 10 (2024), https://doi.org/10.1016/j.heliyon.2024.e37024.
[10] S. Phanichphant, A. Nakaruk, K. Chansaenpak, D. Channei, Evaluating the photocatalytic efficiency of the BiVO4/rGO photocatalyst, Sci. Rep. 9 (2019), https://doi.org/10.1038/s41598-019-52589-5.
[11] L. Xue, F. An, Y. Yang, Y. Ma, Synthesis of N-TiO2/BiOI/RGO composites with significantly enhanced visible light photocatalytic activity, J. Mater. Res. 35 (2020) 153–161, https://doi.org/10.1557/jmr.2019.401.
[12] T.K. Das, M. Jesionek, K. Mistewicz, B. Nowacki, M. Kępińska, M. Zubko, M. Godzierz, A. Gawron, Ultrasonic-assisted conversion of micrometer-sized BiI3 into BiOI Nanoflakes for photocatalytic applications, Int. J. Mol. Sci. 25 (2024), https://doi.org/10.3390/ijms251910265.
[13] K. Dai, D. Li, J. Lv, L. Lu, C. Liang, G. Zhu, A scalable synthesis technique of hierarchical BiOBr microspheres for advanced visible light photocatalyst, Mater. Lett. 136 (2014) 438–440, https://doi.org/10.1016/j.matlet.2014.08.105.
[14] M. Pan, H. Zhang, G. Gao, L. Liu, W. Chen, Facet-dependent catalytic activity of Nanosheet-assembled bismuth Oxyiodide microspheres in degradation of bisphenol a, Enviromental, Science & Technology 49 (2015) 6240–6248, https://doi.org/10.1021/acs.est.5b00626.
[15] X. Gao, X. Zhang, Y. Wang, S. Peng, B. Yue, C. Fan, Rapid synthesis of hierarchical BiOCl microspheres for efficient photocatalytic degradation of carbamazepine under simulated solar irradiation, Chem. Eng. J. 263 (2015) 419–426, https://doi.org/10.1016/j.cej.2014.10.110.
[16] X. Gao, X. Zhang, Y. Wang, S. Peng, B. Yue, C. Fan, Photocatalytic degradation of carbamazepine using hierarchical BiOCl microspheres : Some key operating parameters , degradation intermediates and reaction pathway, Chem. Eng. J. 273 (2015) 156–165, https://doi.org/10.1016/j.cej.2015.03.063.
[17] H. Zhang, Y. Yang, Z. Zhou, Y. Zhao, L. Liu, Enhanced Photocatalytic Properties in BiOBr Nanosheets with Dominantly Exposed (102) Facets, J. Phys. Chem. C 118 (2014) 14662–14669, https://doi.org/10.1021/jp5035079.
[18] M. Arumugam, M.Y. Choi, Recent progress on bismuth oxyiodide (BiOI) photocatalyst for environmental remediation, J. Ind. Eng. Chem. 81 (2020) 237–268, https://doi.org/10.1016/j.jiec.2019.09.013.
[19] J. Jiang, K. Zhao, X. Xiao, L. Zhang, Synthesis and facet-dependent Photoreactivity of BiOCl single- crystalline Nanosheets, J. Am. Chem. Soc. (2012) 8–11.
[20] J. Li, L. Zhang, Y. Li, Y. Yu, Synthesis and internal electric field dependent photoreactivity of Bi 3O4Cl single-crystalline nanosheets with high {001} facet exposure percentages, Nanoscale 6 (2014) 167–171, https://doi.org/10.1039/c3nr05246j.
[21] X. Wu, Y.H. Ng, L. Wang, Y. Du, S.X. Dou, R. Amal, J. Scott, Improving the photo-oxidative capability of BiOBr: via crystal facet engineering, J Mater Chem A Mater 5 (2017) 8117–8124, https://doi.org/10.1039/c6ta10964k.
[22] Y. Mi, M. Zhou, L. Wen, H. Zhao, Y. Lei, A highly efficient visible-light driven photocatalyst: two dimensional square-like bismuth oxyiodine nanosheets, Dalton Trans. 43 (2014) 9549–9556, https://doi.org/10.1039/c4dt00798k.
[23] Y. Chen, J. Fang, S. Lu, Y. Wu, D. Chen, L. Huang, W. Xu, X. Zhu, Z. Fang, Fabrication, characterization and photocatalytic properties of ag/AgI/BiOI

heteronanostructures supported on rectorite via a cation-exchange method, Mater. Res. Bull. 64 (2015) 93–96, https://doi.org/10.1016/j.materresbull.2014.12.040.
[24] R. He, S. Cao, D. Guo, B. Cheng, S. Wageh, A.A. Al-Ghamdi, J. Yu, 3D BiOI-GO composite with enhanced photocatalytic performance for phenol degradation under visible-light, Ceram. Int. 41 (2015) 3511–3517, https://doi.org/10.1016/j.ceramint.2014.11.003.
[25] S. Kang, R.C. Pawar, Y. Pyo, V. Khare, C.S. Lee, Size-controlled BiOCl–RGO composites having enhanced photodegradative properties, J. Exp. Nanosci. 11 (2016) 259–275, https://doi.org/10.1080/17458080.2015.1047420.
[26] R. Vinoth, S.G. Babu, R. Ramachandran, B. Neppolian, Bismuth oxyiodide incorporated reduced graphene oxide nanocomposite material as an efficient photocatalyst for visible light assisted degradation of organic pollutants, Appl. Surf. Sci. 418 (2017) 163–170, https://doi.org/10.1016/j.apsusc.2017.01.278.
[27] V. Mahmoodi, A. Ahmadpour, T.R. Bastami, M.T.H. Mosavian, PVP assisted synthesis of high efficient BiOI/graphene oxide nanohybrid and its photocatalytic performance in degradation of organic dye pollutants, Sol. Energy 176 (2018) 483–495, https://doi.org/10.1016/j.solener.2018.10.056.
[28] M.J. Allen, V.C. Tung, R.B. Kaner, Honeycomb carbon: a review of graphene, Chem. Rev. 110 (2010) 132–145, https://doi.org/10.1021/cr900070d.
[29] K.S. Novoselov, A.K. Geim, S.V. Morozov, D. Jiang, Y. Zhang, S.V. Dubonos, I. V. Grigorieva, A.A. Firsov, Electric field effect in atomically thin carbon films, Science 306 (2016) (1979) 666–669.
[30] W.W. Dai, Z.Y. Zhao, Understanding the interfacial properties of graphene-based materials/BiOI heterostructures by DFT calculations, Appl. Surf. Sci. 406 (2017) 8–20, https://doi.org/10.1016/j.apsusc.2017.02.079.
[31] V. Gladkikh, D.Y. Kim, A. Hajibabaei, A. Jana, C.W. Myung, K.S. Kim, Machine learning for predicting the band gaps of ABX3 perovskites from elemental properties, J. Phys. Chem. C 124 (2020) 8905–8918, https://doi.org/10.1021/acs.jpcc.9b11768.
[32] G. Yu, L. Lyu, F. Zhang, D. Yan, W. Cao, C. Hu, Theoretical and experimental evidence for rGO-4-PP Nc as a metal-free Fenton-like catalyst by tuning the electron distribution, RSC Adv. 8 (2018) 3312–3320, https://doi.org/10.1039/c7ra12573a.
[33] Z. Qu, Y. Su, L. Sun, F. Liang, G. Zhang, Study of the structure, electronic and optical properties of BiOI/rutile-TiO2 heterojunction by the first-principle calculation, Materials 13 (2020), https://doi.org/10.3390/ma13020323.
[34] P. Parida, B. Ganguli, Structural, electronic and optical properties of ZnMnIn2Te 4 chalcopyrite: a DFT + U study, Trans. Indian Inst. Metals 66 (2013) 397–400, https://doi.org/10.1007/s12666-013-0271-9.
[35] Q. Kong, S. Preis, L. Li, P. Luo, C. Wei, Z. Li, Y. Hu, C. Wei, Relations between metal ion characteristics and adsorption performance of graphene oxide: a comprehensive experimental and theoretical study, Sep. Purif. Technol. 232 (2020) 115956, https://doi.org/10.1016/j.seppur.2019.115956.
[36] E.K. Wieduwilt, J.C. Boisson, G. Terraneo, E. Hénon, A. Genoni, A step toward the quantification of noncovalent interactions in large biological systems: the independent gradient model-extremely localized molecular orbital approach, J. Chem. Inf. Model. 61 (2021) 795–809, https://doi.org/10.1021/acs.jcim.0c01188.
[37] L. González-Rodríguez, O. Yáñez, K. Mena- Ulecia, Y. Hidalgo-Rosa, X. García-Carmona, C. Ulloa- Tesser, Exploring the adsorption of five emerging pollutants on activated carbon: a theoretical approach, J. Environ. Chem. Eng. 12 (2024), https://doi.org/10.1016/j.jece.2024.112911.
[38] L. González-Rodríguez, Y. Hidalgo-Rosa, J.O.P. Garcıa, M.A. Treto-Suárez, K. Mena-Ulecia, O. Yañez, Study of heavy metals adsorption using a silicate-based material: experiments and theoretical insights, Chemical Physics Impact 9 (2024), https://doi.org/10.1016/j.chphi.2024.100714.
[39] M.S. Kandanapitiye, M. Gao, J. Molter, C.A. Flask, S.D. Huang, Synthesis, characterization, and X-ray attenuation properties of ultrasmall BiOI nanoparticles: toward renal clearable particulate CT contrast agents, Inorg. Chem. 53 (2014) 10189–10194, https://doi.org/10.1021/ic5011709.
[40] F.A. Bannister, M.H. Hey, The crystal-structure of the bismuth Oxyhalides, Mineral. Mag. 23 (1935) 49–58.
[41] G. Yang, L. Li, W.B. Lee, M.C. Ng, Structure of graphene and its disorders: a review, Sci. Technol. Adv. Mater. 19 (2018) 613–648, https://doi.org/10.1080/14686996.2018.1494493.
[42] M. Ernzerhof, G.E. Scuseria, Assessment of the Perdew-Burke-Ernzerhof exchange-correlation functional, J. Chem. Phys. 110 (1999) 5029–5036.
[43] K.F. Garrity, J.W. Bennett, K.M. Rabe, D. Vanderbilt, Pseudopotentials for high-throughput DFT calculations, Comput. Mater. Sci. 81 (2014) 446–452, https://doi.org/10.1016/j.commatsci.2013.08.053.
[44] L. Bengtsson, Dipole correction for surface supercell calculations, Phys Rev B Condens Matter Mater Phys 59 (1999) 12301–12304, https://doi.org/10.1103/PhysRevB.59.12301.
[45] D.G.A. Smith, L.A. Burns, K. Patkowski, C.D. Sherrill, Revised damping parameters for the D3 dispersion correction to density functional theory, J. Phys. Chem. Lett. 7 (2016) 2197–2203, https://doi.org/10.1021/acs.jpclett.6b00780.
[46] P. Giannozzi, S. Baroni, N. Bonini, M. Calandra, R. Car, C. Cavazzoni, D. Ceresoli, G.L. Chiarotti, M. Cococcioni, I. Dabo, A. Dal Corso, S. Fabris, G. Fratesi, S. De Gironcoli, R. Gebauer, U. Gerstmann, C. Gougoussis, A. Kokalj, M. Lazzeri, L. Martin-Samos, N. Marzari, F. Mauri, R. Mazzarello, S. Paolini, A. Pasquarello, L. Paulatto, C. Sbraccia, S. Scandolo, G. Sclauzero, A.P. Seitsonen, A. Smogunov, P. Umari, R.M. Wentzcovitch, QUANTUM ESPRESSO: a modular and open-source software project for quantum simulations of materials QUANTUM ESPRESSO 2, 2009.
[47] P. Giannozzi, O. Andreussi, T. Brumme, O. Bunau, M. Buongiorno Nardelli, M. Calandra, R. Car, C. Cavazzoni, D. Ceresoli, M. Cococcioni, N. Colonna, I. Carnimeo, A. Dal Corso, S. De Gironcoli, P. Delugas, R.A. Distasio, A. Ferretti, A. Floris, G. Fratesi, G. Fugallo, R. Gebauer, U. Gerstmann, F. Giustino, T. Gorni, J. Jia, M. Kawamura, H.Y. Ko, A. Kokalj, E. Küçükbenli, M. Lazzeri, M. Marsili, N. Marzari, F. Mauri, N.L. Nguyen, H.V. Nguyen, A. Otero-De-La-Roza, L. Paulatto, S. Poncé, D. Rocca, R. Sabatini, B. Santra, M. Schlipf, A.P. Seitsonen, A. Smogunov, I. Timrov, T. Thonhauser, P. Umari, N. Vast, X. Wu, S. Baroni, Advanced capabilities for materials modelling with quantum ESPRESSO, J. Phys. Condens. Matter 29 (2017) 465901, https://doi.org/10.1088/1361-648X/aa8f79.
[48] K. Momma, F. Izumi, VESTA 3 for three-dimensional visualization of crystal, volumetric and morphology data, J. Appl. Cryst. 44 (2011) 1272–1276, https://doi.org/10.1107/S0021889811038970.
[49] M. Saavedra-Torres, F. Toledo, Y. Hidalgo-Rosa, D. Contreras, E. Schott, X. Zarate, Role of Sn atoms on the Crotonaldehyde (2-Butenal) adsorption over bimetallic catalysts PtSn(110), Pt3Sn(111)/Pt(111), Pt3Sn(111) and PtSn4(010): a periodic DFT study, Results Chem 15 (2025), https://doi.org/10.1016/j.rechem.2025.102224.
[50] J.P. Perdew, K. Burke, M. Ernzerhof, Generalized gradient approximation made simple, Phys. Rev. Lett. 77 (1996) 3865–3868, https://doi.org/10.1103/PhysRevLett.77.3865.
[51] A. Schäfer, H. Horn, R. Ahlrichs, Fully optimized contracted Gaussian basis sets for atoms Li to Kr, J. Chem. Phys. 97 (1992) 2571–2577, https://doi.org/10.1063/1.463096.
[52] W.R. Wadt, P.J. Hay, Ab initio effective core potentials for molecular calculations, Potentials for main group elements Na to Bi, J Chem Phys 82 (1985) 284–298, https://doi.org/10.1063/1.448800.
[53] C. Bannwarth, S. Ehlert, S. Grimme, GFN2-xTB—An accurate and broadly parametrized self-consistent tight-binding quantum chemical method with multipole electrostatics and density-dependent dispersion contributions, J. Chem. Theory Comput. 15 (2019) 1652–1671, https://doi.org/10.1021/acs.jctc.8b01176.
[54] C. Bannwarth, E. Caldeweyher, S. Ehlert, A. Hansen, P. Pracht, J. Seibert, S. Spicher, S. Grimme, Extended tight-binding quantum chemistry methods, WIREs Comput. Mol. Sci. 11 (2021) e1493, https://doi.org/10.1002/wcms.1493.
[55] W. Humphrey, A. Dalke, K. Schulten, VMD: Visual molecular dynamics, J. Mol. Graph. 14 (1996) 33–38, https://doi.org/10.1016/0263-7855(96)00018-5.
[56] T. Lu, Q. Chen, Independent gradient model based on Hirshfeld partition: a new method for visual study of interactions in chemical systems, J. Comput. Chem. 43 (2022) 539–555, https://doi.org/10.1002/jcc.26812.
[57] C. Lefebvre, H. Khartabil, J.-C. Boisson, J. Contreras-García, J.-P. Piquemal, E. Hénon, The independent gradient model: a new approach for probing strong and weak interactions in molecules from wave function calculations, ChemPhysChem 19 (2018) 724–735, https://doi.org/10.1002/cphc.201701325.
[58] R.F.W. Bader, A quantum theory of molecular structure and its applications, Chem. Rev. 91 (1991) 893–928, https://doi.org/10.1021/cr00005a013.
[59] R.F.W. Bader, Atoms in Molecules : A Quantum Theory, Clarendon Press, 1990. https://global.oup.com/academic/product/atoms-in-molecules-9780198558651#.WyrPmDy72k4.mendeley (accessed June 19, 2018).
[60] R.F.W. Bader, A Quantum Theory of Molecular Structure and its Appllcatlons, 2025.
[61] T. Lu, F. Chen, Multiwfn: a multifunctional wavefunction analyzer, J. Comput. Chem. 33 (2012) 580–592, https://doi.org/10.1002/jcc.22885.
[62] K.A. Feenstra, B. Hess, H.J.C. Berendsen, Improving efficiency of large time-scale molecular dynamics simulations of hydrogen-rich systems, J. Comput. Chem. 20 (1999) 786–798, https://doi.org/10.1002/(SICI)1096-987X(199906)20:8<786::AID-JCC5>3.0.CO;2-B.
[63] J.-P. Ryckaert, G. Ciccotti, H.J.C. Berendsen, Numerical integration of the cartesian equations of motion of a system with constraints: molecular dynamics of n-alkanes, J. Comput. Phys. 23 (1977) 327–341, https://doi.org/10.1016/0021-9991(77)90098-5.
[64] R. Udayabhaskar, R.V. Mangalaraja, T. Pandiyarajan, B. Karthikeyan, D. Contreras, Spectroscopic investigation on graphene-copper nanocomposites with strong UV emission and high catalytic activity, Carbon N Y 124 (2017) 256–262, https://doi.org/10.1016/j.carbon.2017.08.061.
[65] S. Sun, W. Wang, L. Zhang, Bi2WO6 quantum dots decorated reduced graphene oxide: improved charge separation and enhanced photoconversion efficiency, J. Phys. Chem. C 117 (2013) 9113–9120, https://doi.org/10.1021/jp4004592.
[66] X. Wang, Y. Zhang, C. Zhou, D. Huo, R. Zhang, L. Wang, Hydroxyl-regulated BiOI nanosheets with a highly positive valence band maximum for improved visible-light photocatalytic performance, Appl Catal B 268 (2020) 118390, https://doi.org/10.1016/j.apcatb.2019.118390.
[67] S. Gražulis, A. Daškevič, A. Merkys, D. Chateigner, L. Lutterotti, M. Quirós, N. R. Serebryanaya, P. Moeck, R.T. Downs, A. Le Bail, Crystallography open database (COD): An open-access collection of crystal structures and platform for world-wide collaboration, Nucleic Acids Res. 40 (2012), https://doi.org/10.1093/nar/gkr900.
[68] S. Graulis, D. Chateigner, R.T. Downs, A.F.T. Yokochi, M. Quirós, L. Lutterotti, E. Manakova, J. Butkus, P. Moeck, A. Le Bail, Crystallography open database - An open-access collection of crystal structures, J. Appl. Cryst. 42 (2009) 726–729, https://doi.org/10.1107/S0021889809016690.
[69] M.A. Majeed Khan, R. Siwach, S. Kumar, A.N. Alhazaa, Role of Fe doping in tuning photocatalytic and photoelectrochemical properties of TiO2 for

photodegradation of methylene blue, Opt. Laser Technol. 118 (2019) 170–178, https://doi.org/10.1016/j.optlastec.2019.05.012.
[70] M.A. Majeed Khan, R. Siwach, S. Kumar, M. Ahamed, J. Ahmed, Frequency and temperature dependence of dielectric permittivity/electric modulus, and efficient photocatalytic action of Fe-doped CeO2 NPs, J. Alloys Compd. 856 (2021), https://doi.org/10.1016/j.jallcom.2020.158127.
[71] M. Mousavi, A. Habibi-Yangjeh, M. Abitorabi, Fabrication of novel magnetically separable nanocomposites using graphitic carbon nitride, silver phosphate and silver chloride and their applications in photocatalytic removal of different pollutants using visible-light irradiation, J. Colloid Interface Sci. 480 (2016) 218–231, https://doi.org/10.1016/j.jcis.2016.07.021.
[72] K. Dai, L. Lu, C. Liang, G. Zhu, Q. Liu, L. Geng, J. He, A high efficient graphitic-C3N4/BiOI/graphene oxide ternary nanocomposite heterostructured photocatalyst with graphene oxide as electron transport buffer material, Dalton Trans. 44 (2015) 7903–7910, https://doi.org/10.1039/c5dt00475f.
[73] H. Lu, W. Fan, H. Dong, L. Liu, Dependence of the irradiation conditions and crystalline phases of TiO2 nanoparticles on their toxicity to Daphnia magna, environ Sci, Nano 4 (2017) 406–414, https://doi.org/10.1039/c6en00391e.
[74] J. Ma, F. Yu, L. Zhou, L. Jin, M. Yang, J. Luan, Y. Tang, H. Fan, Z. Yuan, J. Chen, Enhanced adsorptive removal of methyl orange and methylene blue from aqueous solution by alkali-activated multiwalled carbon nanotubes, ACS Appl. Mater. Interfaces 4 (2012) 5749–5760, https://doi.org/10.1021/am301053m.
[75] N. Zibouche, G. Volonakis, F. Giustino, Graphene oxide/perovskite interfaces for photovoltaics, J. Phys. Chem. C 122 (2018) 16715–16726, https://doi.org/10.1021/acs.jpcc.8b03230.
[76] H. Chang, Z. Sun, M. Saito, Q. Yuan, H. Zhang, J. Li, Z. Wang, T. Fujita, F. Ding, Z. Zheng, F. Yan, H. Wu, M. Chen, Y. Ikuhara, Regulating infrared photoresponses in reduced graphene oxide phototransistors by defect and atomic structure control, ACS Nano 7 (2013) 6310–6320, https://doi.org/10.1021/nn4023679.
[77] F. Tian, H. Zhao, Z. Dai, G. Cheng, R. Chen, Mediation of valence band maximum of BiOI by cl incorporation for improved oxidation power in photocatalysis, Ind Eng Chem Res 55 (2016) 4969–4978, https://doi.org/10.1021/acs.iecr.6b00847.
[78] A. Alzamly, M. Bakiro, S.H. Ahmed, S.M. Sallabi, R.A. Al Ajeil, S.A. Alawadhi, H. A. Selem, S.S.M. Al Meshayei, A. Khaleel, N. Al-Shamsi, N. Saleh, Construction of BiOF/BiOI nanocomposites with tunable band gaps as efficient visible-light photocatalysts, J Photochem Photobiol A Chem 375 (2019) 30–39, https://doi.org/10.1016/j.jphotochem.2019.01.031.
[79] F. Dong, Y. Sun, M. Fu, Z. Wu, S.C. Lee, Room temperature synthesis and highly enhanced visible light photocatalytic activity of porous BiOI/BiOCl composites nanoplates microflowers, J. Hazard. Mater. 219–220 (2012) 26–34, https://doi.org/10.1016/j.jhazmat.2012.03.015.
[80] S.S. Kim, T. Van Khai, V. Kulish, Y.H. Kim, H.G. Na, A. Katoch, M. Osada, P. Wu, H.W. Kim, Tunable bandgap narrowing induced by controlled molecular thickness in 2D Mica Nanosheets, Chem. Mater. 27 (2015) 4222–4228, https://doi.org/10.1021/cm504802j.
[81] E.B. Isaacs, C. Wolverton, Performance of the strongly constrained and appropriately normed density functional for solid-state materials, Phys Rev Mater 2 (2018), https://doi.org/10.1103/PhysRevMaterials.2.063801.
[82] J.H. Yuan, Q. Chen, L.R.C. Fonseca, M. Xu, K.H. Xue, X.S. Miao, GGA-1/2 self-energy correction for accurate band structure calculations: the case of resistive switching oxides, J Phys Commun 2 (2018), https://doi.org/10.1088/2399-6528/aade7e.
[83] H. Huang, K. Liu, Y. Zhang, K. Chen, Y. Zhang, N. Tian, Tunable 3D hierarchical graphene-BiOI nanoarchitectures: their in situ preparation, and highly improved photocatalytic performance and photoelectrochemical properties under visible light irradiation, RSC Adv. 4 (2014) 49386–49394, https://doi.org/10.1039/c4ra07533a.
[84] C.J.S.C.S.S.P. Kamakshi, Synthesis, characterization of BiOI/rGO nanocomposite and its photocatalytic functionality analysis under visible light, Inorg. Chem. Commun. 150 (2023) 110545.
[85] H. Liu, W.R. Cao, Y. Su, Z. Chen, Y. Wang, Bismuth oxyiodide-graphene nanocomposites with high visible light photocatalytic activity, J. Colloid Interface Sci. 398 (2013) 161–167, https://doi.org/10.1016/j.jcis.2013.02.007.
[86] H.J. Yan, B. Xu, S.Q. Shi, C.Y. Ouyang, First-principles study of the oxygen adsorption and dissociation on graphene and nitrogen doped graphene for Li-air batteries, J. Appl. Phys. 112 (2012), https://doi.org/10.1063/1.4766919.
[87] F.R. Feret, Determination of the crystallinity of calcined and graphitic cokes by X-ray diffraction, Analyst 123 (1998) 595–600, https://doi.org/10.1039/a707845e.
[88] J. Di, J. Xia, Y. Ge, L. Xu, H. Xu, M. He, Q. Zhang, H. Li, Reactable ionic liquid-assisted rapid synthesis of BiOI hollow microspheres at room temperature with enhanced photocatalytic activity, J Mater Chem A Mater 2 (2014) 15864–15874, https://doi.org/10.1039/c4ta02400a.
[89] Y. Mera, D. Moreno, N. Contreras, M.F. Escalona, R.V. Meléndrez, H. D. Mangalaraja, Mansilla, improvement of the BiOI photocatalytic activity optimizing the solvothermal synthesis, Solid State Sci. 63 (2017) 84–92, https://doi.org/10.1016/j.solidstatesciences.2016.11.013.
[90] B. Andonovic, A. Ademi, A. Grozdanov, P. Paunović, A.T. Dimitrov, Enhanced model for determining the number of graphene layers and their distribution from X-ray diffraction data, Beilstein, Journal of Nanotechnology 6 (2015) 2113–2122, https://doi.org/10.3762/bjnano.6.216.
[91] C.S. Guo, M. Ge, L. Liu, G. Gao, Y. Feng, Y. Wang, Directed synthesis of mesoporous TiO2 microspheres: catalysts and their photocatalysis for bisphenol a degradation, Environ. Sci. Technol. 44 (2010) 419–425, https://doi.org/10.1021/es9019854.
[92] C. Liao, Z. Ma, X. Chen, X. He, J. Qiu, Controlled synthesis of bismuth oxyiodide toward optimization of photocatalytic performance, Appl. Surf. Sci. 387 (2016) 1247–1256, https://doi.org/10.1016/j.apsusc.2016.06.140.
[93] J.F. Escobedo, E.N. Gomes, A.P. Oliveira, J. Soares, Ratios of UV, PAR and NIR components to global solar radiation measured at Botucatu site in Brazil, renew, Energy 36 (2011) 169–178, https://doi.org/10.1016/j.renene.2010.06.018.
[94] B. Long, Y. Huang, H. Li, F. Zhao, Z. Rui, Z. Liu, Y. Tong, H. Ji, Carbon Dots Sensitized BiOI with Dominant {001} Facets for Superior Photocatalytic Performance, Ind. Eng. Chem. Res. 54 (2015) 12788–12794, https://doi.org/10.1021/acs.iecr.5b02780.
[95] J.E.D. Davies, VIBRATIONAL SPECTROSCOPY-III [1] AND RAMAN SPECTRA OF THE BISMUTH(Ill) OXIDE HALIDES, Pergamon Press, 1973.
[96] X. Xiao, Y. Lin, B. Pan, W. Fan, Y. Huang, Photocatalytic degradation of methyl orange by BiOI/Bi4O5I2 microspheres under visible light irradiation, Inorg Chem Commun 93 (2018) 65–68, https://doi.org/10.1016/j.inoche.2018.05.009.
[97] K. Bustos-Ramirez, C.E. Barrera-Diaz, M. De Icaza, A.L. Martínez-Hernández, C. Velasco-Santos, Photocatalytic activity in phenol removal of water from graphite and graphene oxides: effect of degassing and chemical oxidation in the synthesis process, J. Chem. 2015 (2015), https://doi.org/10.1155/2015/254631.
[98] X. Yu, J. Shi, L. Feng, C. Li, L. Wang, A three-dimensional BiOBr/RGO heterostructural aerogel with enhanced and selective photocatalytic properties under visible light, Appl. Surf. Sci. 396 (2017) 1775–1782, https://doi.org/10.1016/j.apsusc.2016.11.219.
[99] I. Childres, L.A. Jaureguib, W. Parkb, H. Caoa, Y.P. Chena, "Raman spectroscopy of graphene and related materials," in New Developments in Photon and Materials Research, Nova Scien, NY, USA, 2013.
[100] S. Vadivel, M. Vanitha, A. Muthukrishnaraj, N. Balasubramanian, Graphene oxide-BiOBr composite material as highly efficient photocatalyst for degradation of methylene blue and rhodamine-B dyes, Journal of water, Process. Eng. 1 (2014) 17–26, https://doi.org/10.1016/j.jwpe.2014.02.003.
[101] F.J. Zhang, F.Z. Xie, W.J. Xie, C.X. Zhu, Graphene/BiOI composites synthesized via the oil bath method and their application for efficient photocatalytic degradation of methyl orange under visible light irradiation, Kinet. Catal. 57 (2016) 339–343, https://doi.org/10.1134/S0023158416030162.
[102] Z.D. Wei, R. Wang, Hierarchical BiOBr microspheres with oxygen vacancies synthesized via reactable ionic liquids for dyes removal, Chin. Chem. Lett. 27 (2016) 769–772, https://doi.org/10.1016/j.cclet.2016.03.013.
[103] Y. Y.H. L.H. Z.Q. Z.Z. P.W, L.H. Yang, Synergistic photocatalytic-Photothermal contribution to antibacterial activity in BiOI-graphene oxide nanocomposites, ACS Appl. Bio Mater. 1 (2018) 2141–2152.
[104] Y. Zhu, X. Liu, K. Yan, J. Zhang, A cathodic photovoltammetric sensor for chloramphenicol based on BiOI and graphene nanocomposites, Sens Actuators B Chem 284 (2019) 505–513, https://doi.org/10.1016/j.snb.2018.12.160.
[105] Y.H. Si, Y. Xia, S.K. Shang, X.B. Xiong, X.R. Zeng, J. Zhou, Y.Y. Li, Enhanced visible light driven photocatalytic behavior of BiFeO3/reduced graphene oxide composites, Nanomaterials 8 (2018), https://doi.org/10.3390/nano8070526.